CHEMISTRY OF MATERIALS

pubs.acs.org/cm

Article

Accurately Determining the Phase Transition Temperature of $CsPbI_3$ via Random-Phase Approximation Calculations and Phase-Transferable Machine Learning Potentials

Tom Braeckevelt, Ruben Goeminne, Sander Vandenhaute, Sander Borgmans, Toon Verstraelen, Julian A. Steele, Maarten B. J. Roeffaers, Johan Hofkens, Sven M. J. Rogge,* and Veronique Van Speybroeck*

Cite This: *Chem. Mater.* 2022, 34, 8561−8576

Read Online

ACCESS | Metrics & More | Article Recommendations | Supporting Information

ABSTRACT: While metal halide perovskites (MHPs) have shown great potential for various optoelectronic applications, their widespread adoption in commercial photovoltaic cells or photosensors is currently restricted, given that MHPs such as $CsPbI_3$ and $FAPbI_3$ spontaneously transition to an optically inactive nonperovskite phase at ambient conditions. Herein, we put forward an accurate first-principles procedure to obtain fundamental insight into this phase stability conundrum. To this end, we computationally predict the Helmholtz free energy, composed of the electronic ground state energy and thermal corrections, as this is the fundamental quantity describing the phase stability in polymorphic materials. By adopting the random phase approximation method as a wave function-based method that intrinsically accounts for many-body electron correlation effects as a benchmark for the ground state energy, we validate the performance of different exchange-correlation functionals and dispersion methods. The thermal corrections, accessed through the vibrational density of states, are accessed through molecular dynamics simulations, using a phase-transferable machine learning potential to accurately account for the MHPs' anharmonicity and mitigate size effects. The here proposed procedure is critically validated on $CsPbI_3$, which is a challenging material as its phase stability changes slowly with varying temperature. We demonstrate that our procedure is essential to reproduce the experimental transition temperature, as choosing an inadequate functional can easily miss the transition temperature by more than 100 K. These results demonstrate that the here validated methodology is ideally suited to understand how factors such as strain engineering, surface functionalization, or compositional engineering could help to phase-stabilize MHPs for targeted applications.

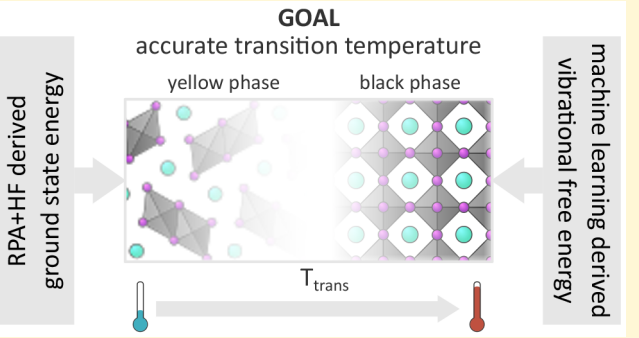

1. INTRODUCTION

Metal halide perovskites (MHPs) hold great potential for various optoelectronic applications, such as solar cells, LEDs, and X-ray imaging,[1−3] thanks to their excellent absorption properties, long charge carrier diffusion lengths, tunable properties, easy synthesis, and low cost.[4−7] Initially, research on MHPs focused on $MAPbI_3$ (MA = methylammonium) and $FAPbI_3$ (FA = formamidinium).[8−11] Later, a chemically more diverse MHP space has been synthesized and investigated in the continuous search to optimize their optoelectronic properties,[12,13] ranging from substituting MA^+/FA^+, Pb^{2+}, and I^- with other ions or ionic complexes to even more complex structures like double MHPs and 2D (Ruddlesden−Popper) MHPs.[14−18] However, despite this versatility in available MHPs, their poor phase stability remains a major hurdle for their widespread commercialization. While the black phases or perovskite phases of these materials—referring collectively to the α, β, and γ phases—attain very attractive optoelectronic properties, they easily transform to the optically inactive δ phase or yellow phase upon cooling to room temperature, both under atmospheric conditions[19−21] and in vacuo,[22−26] as visualized in Figure 1. For instance, the perovskite phase of $CsPbI_3$ is stable only at high temperatures; cooling to room temperature renders the perovskite phase metastable and induces a transformation to the nonperovskite δ_{Cs} phase. A similar phase transformation occurs in $FAPbI_3$, for which cooling leads to the δ_{FA} phase. The latter differs from

Received: May 19, 2022
Revised: August 17, 2022
Published: September 22, 2022

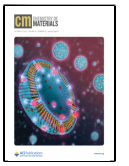

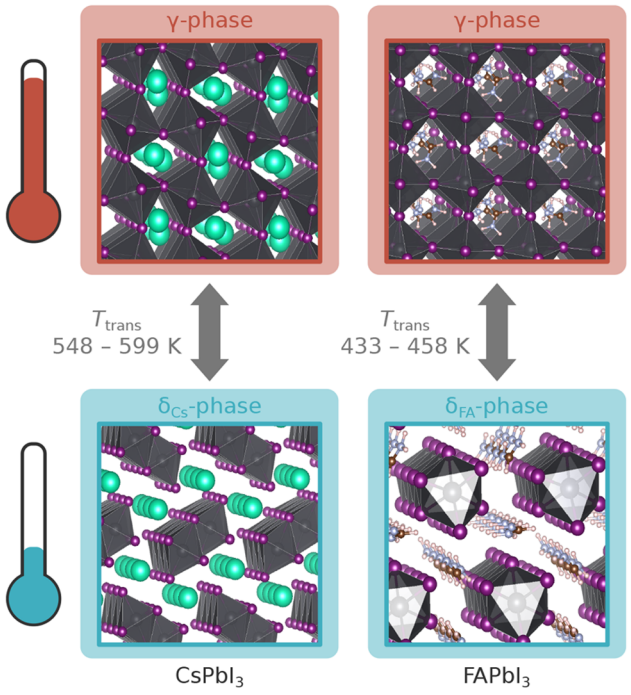

Figure 1. At high temperatures, both $CsPbI_3$ and $FAPbI_3$ adopt their perovskite (α, β, or γ) phase. Below 548 K ($CsPbI_3$) or 433 K ($FAPbI_3$) and, hence, also at room temperature, a nonperovskite δ phase is formed. Because the PbI frameworks of these δ phases differ, the subscript "Cs" or "FA" is added in this paper when referring to the phase which has the PbI framework of the δ phase of $CsPbI_3$ or $FAPbI_3$, respectively. Transition temperatures obtained from refs 24 and 42−45.

the δ_{Cs} phase by the connectivity of the PbI framework. Therefore, extensive attention has been devoted in recent years to find methods to lower the transition temperature from the perovskite to the nonperovskite phase and stabilize the perovskite phase at room temperature. This can be achieved through, e.g., surface functionalization, crystal size control, interface-induced strain engineering, and compositional engineering.[27−35] Given that it is challenging to experimentally isolate these different stabilizing effects, computational modeling has proven to be a necessary and complementary tool to understand the phase stability in MHPs and other materials.[36−41] However, the accuracy of such an endeavor strongly depends on the computational techniques adopted in the procedure. In particular, an accurate prediction of the transition temperature from the perovskite to the nonperovskite phases and vice versa strongly depends on the level of theory used to determine the ground state energies and on the computational approach to determine the thermal corrections. A methodology to accurately determine the transition temperature in MHPs is highly desirable yet still lacking at the moment. In this work, we aim to tackle this challenge by establishing such a computational methodology that can accurately describe the phase stability of a wide range of MHPs, focusing on factors such as the applied level of theory and the supercell size. By critically examining the phase stability of $CsPbI_3$, we demonstrate that these are crucial elements to obtain an accurate prediction of both the ground state energy and the thermal corrections to the free energy, which dictate the phase stability in MHPs.

Density functional theory (DFT) has proven to be the first-principles method of choice to computationally model realistic materials, given its exceptional trade-off between computational efficiency and accuracy, especially when compared to wave function-based Hartree−Fock (HF) calculations.[46−50] Conceptually, DFT yields the exact ground state energy, if the exact exchange correlation (XC) functional were known. In practice, however, the choice of the XC functional introduces errors which may substantially impact the results and thus the prediction of the stability of the different phases for a given material. To quantify these errors, several MHP benchmark studies have been performed, indicating that expensive many-body methods, such as the Green's function many-body perturbation approach (GW), are necessary to accurately calculate the electronic density of states.[51−55] Luckily, predicting the ground state energy, which is needed to assess the stability, is typically less demanding. Bokdam and co-workers benchmarked the performance of different XC functionals in predicting the ground state energy of the $MAPbI_3$ perovskite phases, applying the random-phase approximation (RPA) to the correlation energy as in refs 56 and 57. While substantially more expensive than DFT, RPA is in principle a fully *ab initio* method that can be regarded as the golden standard to obtain accurate ground state energies. In their work, Bokdam et al. revealed that SCAN, HSE, and HSE +D3 are the best XC functionals that most closely approach the RPA results when predicting the energy differences between structures generated via MD simulations of the γ phase of $MAPbI_3$. However, to determine the phase transition temperature, the difference in ground state energies between the competing perovskite and nonperovskite phases is an even more important property than the ground state energy difference between states in the perovskite phase.[58] To date, it remains unclear which XC functional performs best in accurately predicting ground state energy differences between the perovskite and nonperovskite phases for MHPs. Therefore, in our approach to determine accurate phase transition temperatures, we will extensively benchmark how different XC functionals and dispersion methods reproduce the ground state energy differences among the γ, δ_{Cs}, and δ_{FA} phases of $CsPbI_3$, compared to RPA+HF results which will be taken as the golden standard. We explicitly consider the δ_{FA} phase, observed experimentally only in $FAPbI_3$ until now, as well for $CsPbI_3$ to highlight the transferability of the here proposed procedure. Because $CsPbI_3$ is a soft material,[59] the phase space will be explored beyond the expected ground state with molecular dynamics (MD) simulations to find the global minimum for which accurate ground state energies will be calculated. Finally, the effect of spin−orbit coupling (SOC) on the ground state energy will be accounted for.

Besides accurately predicting the ground state energy difference, the envisaged computational methodology should also incorporate thermal effects in order to understand the phase behavior at operating temperatures. Therefore, a second task in determining accurate phase transition temperatures is to obtain the vibrational contributions to the free energy, going beyond the harmonic oscillator approximation to account for anharmonic effects present in these materials.[60,61] The common approach to predict the vibrational free energy is by calculating the vibrational density of states (VDOS) from small ionic displacements and subsequently applying the harmonic approximation to obtain the free energy.[62,63] However, this method does not include any anharmonic

https://doi.org/10.1021/acs.chemmater.2c01508
Chem. Mater. 2022, 34, 8561−8576

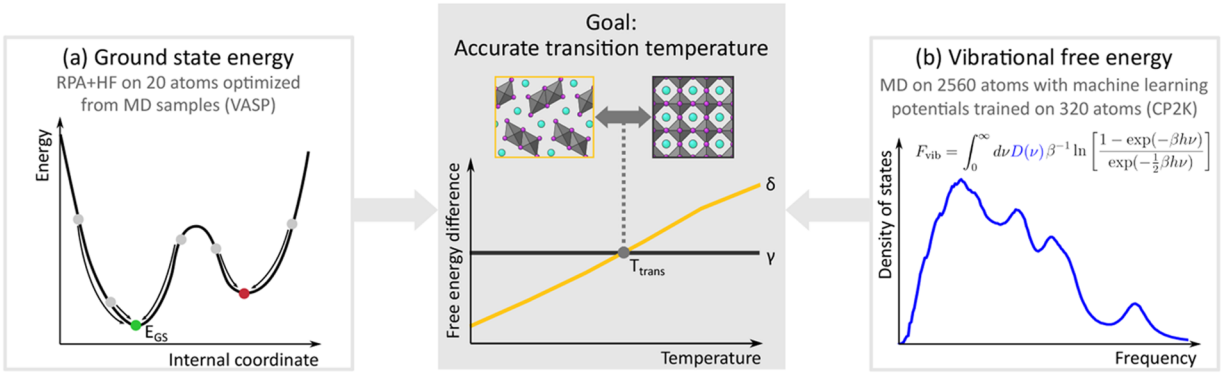

Figure 2. Schematic depiction of our approach to accurately determine the transition temperature in MHPs. The free energy is decomposed into two parts that are calculated separately: (a) The ground state energy for which RPA+HF calculations were performed with VASP on structures of 20 atoms. These ground state structures were optimized starting from different snapshots of an MD simulation. (b) The vibrational free energy for which the vibrational density of states was calculated from NVE MD simulations with a machine learning potential that was derived from CP2K calculations on 320-atom supercells.

effects, which are present for $CsPbI_3$ given that the material exhibits several low-frequency modes.[41] To account for temperature-dependent anharmonic effects, the frequencies will here be determined by calculating the velocity autocorrelation function from an MD run at a specific temperature instead.[64] The VDOS for different phases of $CsPbI_3$ has been calculated before, via static[65,66] and recently also via MD calculations.[66,67] Kaiser and co-workers performed MD calculations of the perovskite phase at 450 K and used velocity autocorrelation functions to obtain the VDOS. However, they performed their calculations on a relatively small 320-atom supercell. Gu et al. calculated the VDOS of the γ and δ_{Cs} phases from 300 to 700 K via mode-projected velocity-autocorrelation functions,[66,68] which differ from regular velocity autocorrelation functions as they require a finite q-point grid.[69] Moreover, they performed calculations on supercells of 160 atoms, whereas we will show herein that supercells containing more than 1000 atoms and simulation times exceeding 10 ps are needed to ensure convergence of the VDOS has been reached. Combining such length and time scales is unfeasible at the DFT level.[64,69−73] Therefore, to calculate thermal effects in this work, a machine learning potential (MLP) will be trained for the γ, δ_{Cs}, and δ_{FA} phases of $CsPbI_3$ with SchNetPack[74] to increase the accessible size and length scale of our simulations. Afterward, this MLP will be adopted to perform MD simulations at temperatures between 100 and 600 K, from which the velocity autocorrelation functions and the temperature-dependent VDOS will be extracted. From these VDOS, the vibrational free energy as a function of temperature will be determined. Finally, we will critically evaluate the sensitivity of the finally obtained free energies on the MLP parameters, the supercell sizes, the lengths of the MD trajectories, and the required training data.

Ultimately, by combining accurate electronic ground state energies complemented with vibrational free energies, we will predict the γ-to-δ_{Cs} phase transition temperature. To demonstrate the MLP's reliability, the total free energy obtained with the MLP will be compared with DFT results obtained on a smaller unit cell. Finally, the validity of the here proposed methodology will be critically assessed by comparing with the experimentally found transition temperatures, revealing a remarkably good correspondence and providing confidence in the accuracy of the proposed approach to untangle the different effects impacting the phase stability in MHPs.

2. THEORETICAL FRAMEWORK

From a thermodynamic point of view, the most stable phase at a given temperature is the one with the lowest Helmholtz free energy. This free energy consists of the ground state energy on the one hand and the vibrational free energy on the other hand, as shown in Figure 2. Section 2.1 introduces both contributions and explains the decomposition. The applied methodologies to accurately calculate the ground state energy and the vibrational free energy are discussed in Section 2.2 and 2.3, respectively.

Adding both contributions together results in the total Helmholtz free energy, which is calculated at multiple temperatures for each of the different phases. The transition temperature then immediately follows as that temperature at which the total free energy of the yellow phase and the total free energy of the black phase coincide, as shown schematically in Figure 2.

2.1. Decomposing the Free Energy at Finite Temperature. The Helmholtz free energy F can be separated into different contributions:

$$F = E_{GS} + F_{trans} + F_{vib} + F_{elec} \approx E_{GS} + F_{vib} \quad (2.1)$$

In this expression, E_{GS} is the electronic ground state energy and F_{trans} is the free energy due to global translations, which is the same for each phase. As we are only interested in the relative energy difference between the different phases, F_{trans} is omitted here, which is enforced practically by removing the center-of-mass velocity of the unit cell. F_{elec} is the free energy contribution due to the electrons, which can be neglected because the band gap for all phases of $CsPbI_3$ is substantially higher than k_BT, with k_B being the Boltzmann constant and T the temperature. At room temperature, k_BT = 26 meV, and the phase with the smallest band gap, the γ phase, has a band gap of 1.56 eV.[75] Therefore, F_{vib}, the free energy due to molecular vibrations, is in good approximation the only temperature- and phase-dependent component in the total Helmholtz free energy.[61]

The first term in eq 2.1, the ground state energy, corresponds with the electronic energy at 0 K, which is found by solving the many-body Schrödinger equation for the

https://doi.org/10.1021/acs.chemmater.2c01508
Chem. Mater. 2022, 34, 8561−8576

atomic positions at 0 K.[70] Within this work, the ground state energy will be calculated with various DFT methods on the one hand, as well as with RPA+HF as the benchmark methodology on the other hand (see Section 2.2).

The second term in eq 2.1, the vibrational free energy, is calculated based on the fundamental normal-mode frequencies of the system at a given temperature, T, by assuming that the vibrational modes of the system behave as noninteracting harmonic oscillators. The total vibrational free energy can then be calculated as the integral over the frequency, ν, of the vibrational density of states (VDOS), $D(\nu)$, multiplied with the vibrational free energy of a quantum harmonic oscillator with frequency ν, $F_{vib}(\nu)$:[64]

$$F_{vib} = \int_0^\infty d\nu\, D(\nu) F_{vib}(\nu) \tag{2.2}$$

with

$$\begin{aligned} F_{vib}(\nu) &= \beta^{-1} \ln\left[\frac{1-\exp(-\beta h\nu)}{\exp\left(-\frac{1}{2}\beta h\nu\right)}\right] \\ &= \beta^{-1} \ln[1 - \exp(-\beta h\nu)] + E_{ZPE}(\nu); \\ E_{ZPE}(\nu) &= \tfrac{1}{2} h\nu \end{aligned} \tag{2.3}$$

In the formula above, h is Planck's constant, $\beta = (k_B T)^{-1}$, and E_{ZPE} is the zero point energy. Zero frequency translational modes are removed according to the procedure described in Section 9 of the Supporting Information (SI). To account for anharmonic effects, the VDOS in eq 2.2 can be calculated as the mass-weighted Fourier transform of the nuclear velocity autocorrelation function:

$$D(\nu) = 2\beta \sum_{j=1}^{N_A} m_j \int_{-\infty}^{\infty} dt \left[\lim_{\tau\to\infty} \frac{1}{2\tau} \int_{-\tau}^{\tau} dt'\, \vec{v}_j(t'+t)\cdot\vec{v}_j(t')\right] \exp(-i2\pi\nu t) \tag{2.4}$$

with N_A the number of atoms and m_j and $\vec{v}_j$ the mass and velocity of atom j, respectively. Integration over the entire VDOS yields the total degrees of freedom (N_f):[64,76]

$$N_f = 3N_A - 3 = \int_0^\infty d\nu D(\nu) \tag{2.5}$$

The velocities in eq 2.4 can be calculated during an NVE MD simulation for which the initial kinetic energy is chosen such that it fluctuates around a specific temperature during the simulation. Via this method, temperature-dependent anharmonic effects are inherently taken into account.

2.2. Ground State Energy Calculations. As shown in Figure 2a, the ground state energy is the first contribution to the total free energy. There are two main challenges to determine the ground state energy with DFT. First, the structure with the lowest energy should be found. Because $CsPbI_3$ is a relatively soft material, its energy surface is characterized by multiple local minima in phase space, corresponding with different energies. For MHPs with even more mobile A-site cations, such as methylammonium (MA^+) and formamidinium (FA^+), this is *a fortiori* the case due to the rotational freedom of the organic cations.[57] To ensure that our procedure succeeds in finding all local minima, we first perform an MD simulation for each optimized phase (the γ, δ_{Cs}, and δ_{FA} phases) that fully scans the phase space around the sought-after minimum. From that trajectory, 101 relevant snapshots are extracted, and their nuclear structure is optimized until their energy has converged. Afterward, the structure with the lowest energy for each phase is selected and used to determine the ground state energy differences between the phases. We furthermore show in Section 4.1 that, due to the softness of $CsPbI_3$, multiple inequivalent γ and δ_{FA} phases can be found in the material and quantify their similarity.

A second challenge in determining the ground state energy of MHPs relates to the accuracy of the used electronic structure method. DFT is ubiquitously used because of its computational efficiency compared to more expensive many-body techniques. However, DFT is very sensitive to the particular choice of the XC functional and dispersion method.[77] In contrast, RPA+HF is a fully first-principles many-body electronic structure method[56,78] which can account for dynamic electronic screening and mid- to long-range dispersion interactions.[79] Therefore, RPA+HF is able to make good predictions for various bond types: it has been demonstrated to well reproduce energy differences of metallic, covalent, ionic, and van der Waals bonds.[56,77−87] As a result, RPA+HF shows a remarkable improvement over DFT for the prediction of the stability of polymorphs.[88,89] Based on these considerations, the RPA+HF energy is chosen as the reference to assess the quality of the DFT results in this work.

Within the adiabatic connection fluctuation−dissipation theorem with the RPA, the total energy of a system is decomposed into two parts:[88]

$$E_{total} = E_{HF} + E_{RPA} \tag{2.6}$$

E_{HF} is the Hartree−Fock total energy calculated non-self-consistently using Kohn−Sham (KS) orbitals, which are determined *a priori* from a DFT calculation. E_{HF} can be separated in four terms: the kinetic energy evaluated with the KS orbitals (T_{KS}), the interaction energy between the electrons and the nuclei (E_{e-n}), the classical Coulomb repulsion between the electrons (the Hartree energy, E_H), and the exact exchange energy (E_x):[88]

$$E_{HF} = T_{KS} + E_{e-n} + E_H + E_x \tag{2.7}$$

E_{RPA} in eq 2.6 is the correlation energy (E_c):

$$E_{RPA} = E_c = \int_0^\infty \frac{d\omega}{2\pi} \mathrm{Tr}\{\ln[1 - \chi(i\omega)V] + \chi(i\omega)V\} \tag{2.8}$$

In this expression, $\chi(i\omega)$ is the independent particle polarizability,[90] V is the Coulomb kernel, and $i\omega$ is the imaginary frequency.[56] RPA+HF is an accurate but also a very expensive method. In view of the need for larger screening studies of MHPs, it is essential to identify computationally less expensive XC functionals, with or without dispersion corrections, that can reproduce the RPA results to a satisfactory extent.

2.3. Vibrational Free Energy Calculations. The second contribution to the total free energy is the vibrational free energy, as depicted in Figure 2b. As demonstrated in eq 2.2, determining the vibrational free energy requires knowledge of the fundamental frequencies in the system. To accurately obtain these frequencies, NVE simulations are the most appropriate as they are not influenced by thermostats or barostats present in other thermodynamic ensembles. For MHPs that contain low-frequency vibrational modes that span multiple unit cells, such as $CsPbI_3$, the simulation time should be long enough and the simulation cell should be large enough to ensure sufficient sampling. This was already shown in previous works[64,69−73] and is confirmed in this work as well,

https://doi.org/10.1021/acs.chemmater.2c01508
Chem. Mater. 2022, 34, 8561−8576

more specifically in Section 4.2 of the main paper and Section 10.1 of the SI. These settings are practically unfeasible for DFT calculations.

In principle, classical force fields, which fit an analytic function to the potential energy surface, could be a viable alternative for DFT calculations at finite temperatures. However, while force fields for MHPs exist,[91−93] they have important drawbacks, for example, when describing the rotational dynamics of the MA^+ molecular ion in $MAPbI_3$.[57] Because the goal of this paper is to propose a methodology that is applicable for multiple phases and different MHPs, an approach based on classical force fields is not preferred. Instead, in this paper, machine learning potentials (MLPs) are trained to perform NVE simulations and determine the frequencies. Within the framework of MLPs, a numerical potential is trained based on underlying quantum mechanical data using a nonlinear regression method. It has been shown that MLPs can accurately reproduce first-principles results at a fraction of the cost, if enough training data is provided.[94,95] Moreover, MLPs for MHPs have already been trained successfully, although this field is still in full development.[96−99]

Since we aim to train one MLP that is transferable to multiple phases and because the evaluation of a neural network is independent of the size of the training data set, a neural network is preferred over a kernel regression method.[100] In this paper, SchNetPack[74] is used to train the MLP. SchNet is a deep neural network based on continuous filter convolutions. Training the network on the input data, it can be used to predict energies and forces from the atomic coordinates. To check the desired transferability, four different MLPs are trained. MLP_{all} is trained on the aggregated input data of the γ, δ_{Cs}, and δ_{FA} phases, whereas separate MLP_{γ}, $MLP_{\delta_{Cs}}$, and $MLP_{\delta_{FA}}$ are trained on data only pertaining to that specific phase. Given our goal to derive a phase-transferable MLP, we will investigate the ability of MLP_{all} to describe all phases simultaneously with an accuracy similar to those of the MLPs trained on the individual phases.

Given that the unit cell remains fixed during the NVE simulations, it is important to select a proper initial structure. To this end, and as explained in more detail in Section 3, an NPT simulation is performed first to determine a physically sensible unit cell, and this structure is then used as input for an NVT simulation at the target temperature to obtain the initial structure of the NVE simulations performed in this work. Using the obtained NVE trajectory, the VDOS at the required temperature is calculated using eq 2.4, which is then used to determine the total vibrational free energy through eqs 2.2 and 2.3.

3. METHODS

Section 1 of the SI details the schematic flowchart that was applied to determine the total Helmholtz free energy. The flowchart contains the different computational steps, which are explained in more detail in this section.

3.1. Determining the Ground State Energy with VASP. All calculations to determine the ground state energy are performed with VASP,[101,102] for which the Cs_sv ($5s^25p^66s^1$), Pb_d ($5d^{10}6s^26p^2$), and I ($5s^25p^5$) projected augmented wave functions (PAW) PBE potentials are used.[103] As confirmed in Section 2.5 of the SI, the RPA+HF results obtained using PAW PBE potentials are comparable to those obtained using PAW GW potentials, which differs from earlier observations by Cui et al.[88] The electronic convergence threshold for the energy is set to 10^{-5} eV, and the projection operators are evaluated in reciprocal space. For all calculations, the precision mode is set to "normal", unless mentioned otherwise in Section 2 of the SI. Furthermore, for each calculation, Gaussian smearing with SIGMA = 0.05 and nonspherical contributions related to the gradient of the density in the PAW spheres are adopted. The following XC functionals and dispersion methods are compared: PBE,[104] PBE+D2,[105] PBE+D3(BJ),[106,107] PBE+D3(BJ)^{ATM},[108,109] PBE+TS,[110] PBE+MBD,[111−113] PBE+MBD/FI,[114] PBEsol,[115] vdW-DF2,[116−119] SCAN,[120] SCAN+rVV10,[121] M06-L,[122] HSE06,[123,124] HSE06+D3(BJ), HSE06+D3(BJ)^{ATM}, and RPA+HF.[77] The spin−orbit coupling (SOC) effects are investigated for the PBE and HSE06 XC functionals.[125] In general, the cutoff energy is set to 600 eV, and 4 × 4 × 3, 6× 4 × 2, and 4× 2 × 4 k-point grids are used for the γ, δ_{Cs}, and δ_{FA} phases, respectively. The PBE+MBD(/FI) and RPA+HF calculations deviate from this, as discussed in Section 2 of the SI and in the paragraph below. The following paragraphs discuss in more detail the MD simulations, the geometric optimization, and the RPA +HF single point calculations with VASP. Most settings mentioned here are obtained after convergence tests. The results and the discussion of these tests can be found in full in Section 2 of the SI. The workflow and job management for the VASP calculations were facilitated by an integrated development environment called pyiron, which allowed for a consistent and automated calculation protocol that proved to be easily extendable toward additional computational settings.[126]

3.1.1. Finding Local Minima with NPT Molecular Dynamics and Geometric Optimizations. First, for all three phases (γ, δ_{Cs}, δ_{FA}), separate NPT MD runs of 10 ps are performed at atmospheric pressure (P = 1 bar) and at T = 600 K. The main goal of these MD calculations is to sample a representative part of the phase space and to identify any secondary minima around the three phases. These calculations are run on low settings, i.e., using the PBE+D3(BJ) XC functional, a cutoff energy of 400 eV and 3 × 3 × 2, 5× 3 × 2, and 3× 2 × 3 k-point grids for the γ, δ_{Cs}, and δ_{FA} phases, respectively. These settings are chosen because the accuracy of these MD calculations is of lesser importance when exploring the phase space, in contrast to the single point calculations performed afterward to accurately determine the ground state energies. The MD calculations are performed with a Verlet time step of 0.5 fs and using a Langevin thermostat with a friction coefficient of 10 ps^{-1} for all atoms and lattice parameters.[127,128]

From the obtained MD trajectories, one snapshot is taken every 0.1 ps yielding 101 snapshots for each phase (including the initial structure) in total. Afterward, a geometric optimization is performed on each snapshot, using a conjugate gradient algorithm to update the positions, volume, and unit cell shape until the energy is converged within 0.1 meV. The PBE+D3(BJ) XC functional is adopted to calculate the energy and the forces, with a step width scaling of 0.5. These calculations are computationally much more expensive than single point energy calculations, as typically a few hundred steps are necessary to reach convergence. This is unfeasible for the RPA+HF calculations.[88] Therefore, the optimization is only performed with the PBE+D3(BJ) XC functional.

3.1.2. Performing High Level RPA+HF Calculations. The settings of the RPA+HF calculations are carefully tested and discussed in Section 2.5 of the SI. In contrast to the regular settings, the cutoff energy is decreased to 400 eV, and the k-point grid for the δ_{FA} phase is increased to 4 × 3 × 4. Decreasing the cutoff energy has almost no effect on the ground state energy and makes the calculations substantially less computationally expensive. The k-point grid of the δ_{FA} phase is changed such that it has the same k-point density as the γ and δ_{Cs} phases; see also Figures S16 and S19. The correlation energy is calculated with the cubic scaling space-time RPA algorithm implemented in VASP,[129,130] for which eight (imaginary) frequency and imaginary time grid points are used. The correlation energy is calculated through eq 2.8 using DFT orbitals obtained with the PBE XC functional to determine the $\chi(i\omega)$ independent particle polarizability. The correlation energy is extrapolated to the limit of infinite cutoff energy by linearly regressing eight evaluated correlation energies determined with eight different cutoff energies, which is the traditional approach implemented in VASP to overcome the slow

https://doi.org/10.1021/acs.chemmater.2c01508
Chem. Mater. 2022, 34, 8561−8576

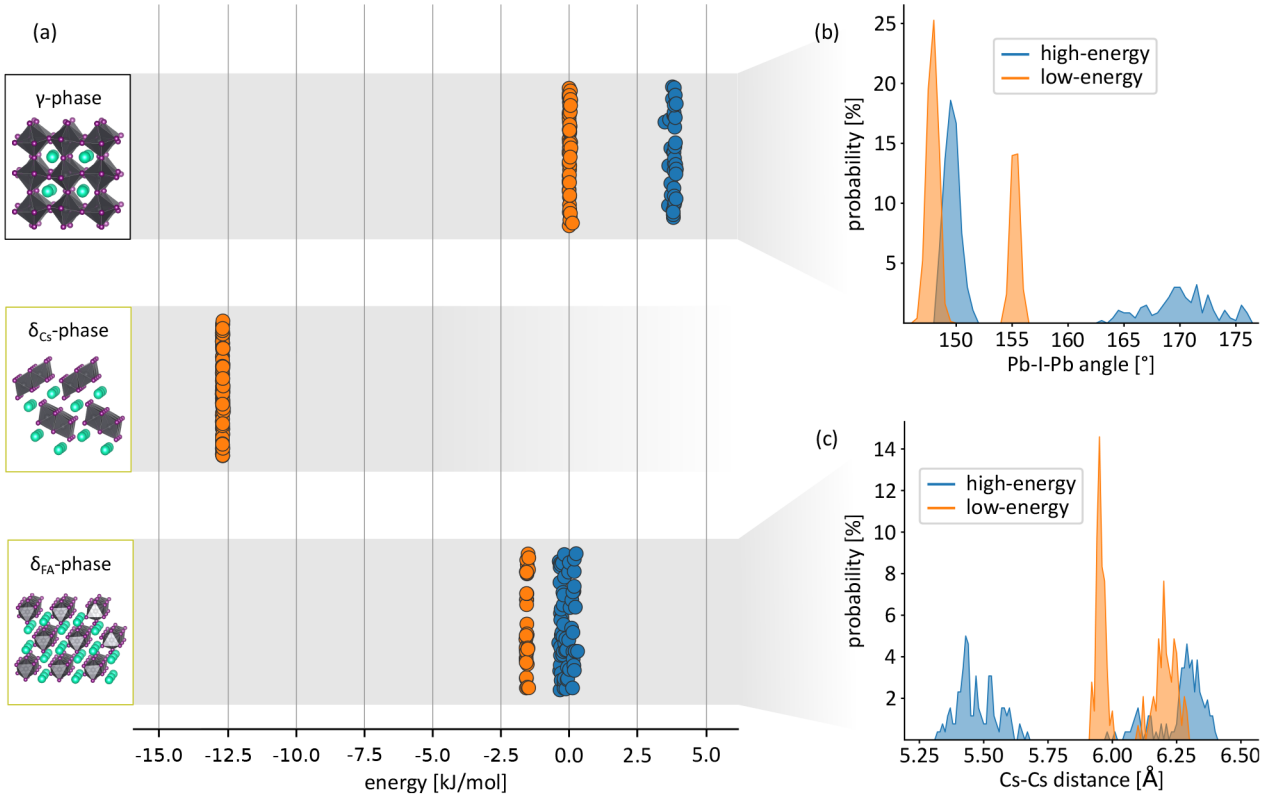

Figure 3. (a) Energy of all optimized structures for the three phases, calculated with DFT using the PBE+D3(BJ) XC functional. For the δ_{Cs} phase, all structures have approximately the same energy, while for the γ and δ_{FA} phases two separate groups of structures with similar energies are identified by a different color. (b) Pb−I−Pb bond angle distribution for each structure of both groups for the γ phase. (c) Cs−Cs distance distribution for each structure of both groups for the δ_{FA} phase.

convergence of the correlation energy with respect to the cutoff energy.[131] The precision of the fast Fourier transform (FFT) grids used in the cubic scaling space-time RPA routines is set to "Fast". The exact exchange part of eq 2.7 is evaluated in this paper using the DFT orbitals obtained with the PBE XC functional and a "Normal" precision of the FFT grids.

3.2. Determining the Vibrational Free Energy with CP2K and Machine Learning Potentials. All calculations related to the input data for the MLPs and their validity are performed with CP2K.[132,133] The energy and forces of the MD and single point calculations are calculated with DFT using the PBE+D3(BJ) XC functional unless mentioned otherwise. CP2K adopts a combined Gaussian and plane wave basis set to determine the wave function, using the GTH pseudopotentials and TZVP-MOLOPT-SR-GTH basis sets.[134−136] The cutoff energy and relative cutoff are set to 400 and 40 Ry, respectively. All calculations are performed on a 320-atom supercell with a single k-point, the Γ-point. For the NVT and NPT simulations, the temperature is controlled with a Nosé−Hoover thermostat with a time constant of 100 fs and three thermostat beads.[137−139] For the NPT simulations, also an MTK barostat with a time constant of 500 fs is adopted to control the pressure at 1 bar.[140] Convergence tests for the input settings of these CP2K calculations are reported and discussed in Section 3 of the SI.

3.2.1. Generating the Training Data for the Machine Learning Potentials. The input DFT data to train the MLP, i.e., the energies and atomic forces, are generated with CP2K. First, for each phase, four different structures are constructed with an initial NPT (P = 1 bar and T = 600 K) simulation using a 320-atom supercell as the initial structure. Second, each of these four structures is used as the initial structure for 11 NPT simulations with P = 1 bar and T = 300, 350, 400, 450, 500, 550, 600, 650, 700, 750, or 800 K. Using different temperatures ensures a more diverse sampling of the phase space and an increased transferability in the temperature window from 100 to 600 K. It is necessary to augment the sampled phase space with NPT structures generated at temperatures higher than 600 K as the NVE simulations with the MLP at 600 K were unstable otherwise. Finally, for every NPT simulation, one snapshot is extracted every 10 fs to train the MLP. This is done to suppress correlations in the data. The final training set consists of 189 268 snapshots in total.

3.2.2. Training and Validating the Machine Learning Potentials. The MLP is trained with SchNetPack.[74] A SchNet model with 128 features, 6 interaction blocks, 50 Gaussians, and a cosine cutoff function with a cutoff of 6 Å is used. The model is trained with a batch size of 32. The model is trained on the energies and forces using the Adam optimization algorithm with a dimensionless learning rate of 5×10^{-5}.[141] The MLP did not learn the stresses because they increased the mean absolute error of the forces. In addition, reproducing the stresses is only vital when performing NPT simulations, which is not necessary to derive the vibrational free energy here. In the loss function, the energy loss is multiplied with 1×10^{-4} and the loss of the forces with 1, to account for the different scales of energy and forces. The model trained for approximately 9 days on 1 NVIDIA Volta V100 graphics processing unit. The MLP parameters mentioned in this paragraph are chosen after scanning the parameter space. The results of these tests can be found in Section 4.1 of the SI. The cutoff radius has the most significant effect on the mean absolute error (MAE) of the forces. Therefore, the effect of the cutoff radius on the VDOS is investigated in Section 10.3 of the SI.

The effect of training on all phases simultaneously or, conversely, of training an MLP for each phase separately, on the VDOS and the vibrational free energy will be discussed in Section 4.2. In Section 4.3 of the SI, the NVE MD simulations performed with the MLP are validated by calculating the MAE of the forces and by comparing the histograms of the Pb−I distances and the Pb−I−Pb angles to those obtained with CP2K.

3.2.3. Initializing the NVE Molecular Dynamics Simulations. Before the NVE simulations are performed, the unit cell and total

https://doi.org/10.1021/acs.chemmater.2c01508
Chem. Mater. 2022, 34, 8561−8576

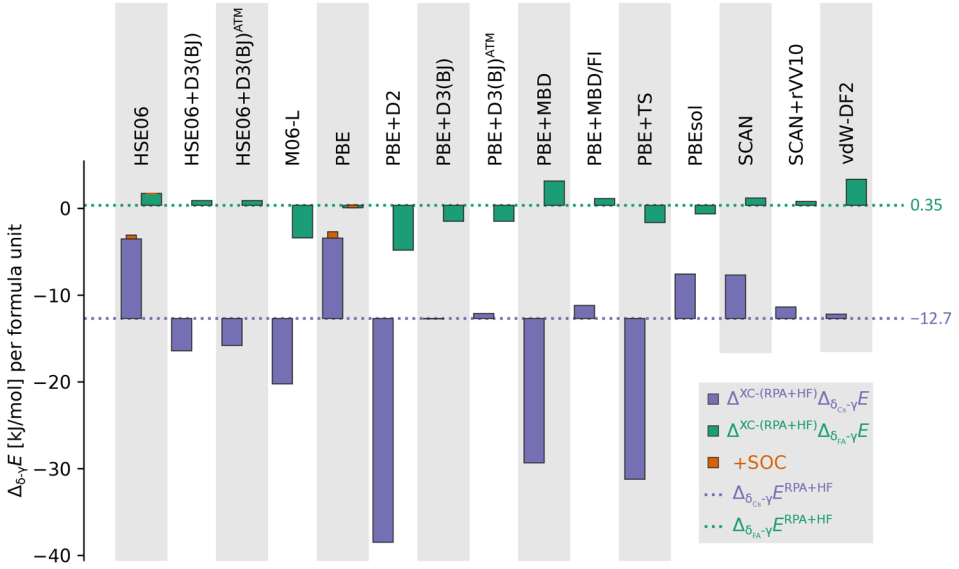

Figure 4. Ground state energy difference between either the δ_{Cs} (purple, $\Delta_{\delta_{Cs}-\gamma}E$) or the δ_{FA} phase (green, $\Delta_{\delta_{FA}-\gamma}E$) and the γ phase as a function of the used XC functional. The dotted lines indicate the results of the reference RPA+HF calculations ($\Delta_{\delta-\gamma}E^{RPA+HF}$, purple for δ_{Cs} and green for δ_{FA}), while the bars quantify, for each XC functional, the difference with respect to this RPA+HF reference ($\Delta^{XC-(RPA+HF)}\Delta_{\delta-\gamma}E$). Each bar starts at RPA+HF results and ends at the calculated value for that XC functional. The orange bar reveals the extra correction to the ground state energy differences for the PBE and HSE06 XC functionals due to the inclusion of spin−orbit coupling (SOC).

energy of the system need to be determined for each phase and at each desired temperature. The temperatures of 100, 200, 300, 400, 500, and 600 K are chosen, as these encompass the expected transition temperature, depicted in Figure 1.

First, the unit cell is determined for each phase by performing NPT simulations with CP2K at the desired temperature and at P = 1 bar. The first 3 ps are discarded as the equilibration time, whereas the following 10 ps or more are used to determine the unit cell. This is done by averaging each unit cell parameter and by globally rescaling the cell lengths such that the new unit cell volume equals the average unit cell volume during the NPT simulation.

Second, to ensure that the average temperature throughout the NVE simulation approximately equals the desired temperature, the initial velocities are rescaled to obtain the target average kinetic energy at that temperature, $E_{kin} = \frac{3N_A k_B T}{2}$. In addition, to obtain an equilibrated starting structure, the initial structure for the NVE simulation is extracted from the final snapshot of a converged NVT simulation (simulation time of approximately 14 ps) at the desired temperature and with the cell parameters extracted from the NPT simulation.

The effect of the length of the NVE MD runs is discussed in Section 10.1 of the SI. The MD runs are 1 ns long for the MLP, except for the 20 480-atom supercell, for which the simulation time is reduced to 500 ps. For the CP2K MD simulations, the simulation time is 24 ps per simulation. To reduce the noise in the spectra, the average VDOS of eight such MD runs is calculated, as discussed in Section 11 of the SI.

4. RESULTS

4.1. Ground State Energy. *4.1.1. Finding the Global Minima.* The first step to determine the ground state energy is to find the structure with the lowest energy. To this end, we follow the procedure outlined in Section 2.2 and calculate, for each phase, the 0 K energy for 101 optimized snapshots encountered during an NPT MD run. Figure 3a visualizes the calculated energies of all optimized structures for the three phases using the PBE+D3(BJ) XC functional. Only for the δ_{Cs} phase do all optimizations converge to approximately the same energy. This contrasts with the γ and δ_{FA} phases, for which different optimized energies can be found depending on the initial structure. For both phases, we can identify two groups of structures that have a similar energy, as indicated by the different colors in Figure 3a.

To explain these energetic differences and to explore whether structures with a similar energy are approximately the same, Figure 3b shows two histograms, one for the low-energy structures and one for the high-energy structures, containing the Pb−I−Pb bond angles for each of the 101 optimized structures in the γ phase. Analogously, Figure 3c reveals two histograms for the Cs−Cs distance of all 101 optimized structures in the δ_{FA} structures. In both cases, the histograms of the high- and low-energy structures reveal clear structural differences, which correlate well with the energy differences between them. To investigate whether the structures within a group are very similar, Figure S26 visualizes the histograms of the Pb−I−Pb bond angle and Cs−Cs distance for six low-energy structures of the γ and δ_{FA} phases, respectively. These histograms differ only by approximately 1° for the γ phase and 0.1 Å for the δ_{FA} phase, indicating that these optimized structures have almost no structural differences. The same is true when considering different high-energy structures, which only reveal slightly wider peaks due to the slightly larger spread on the optimized energies and the larger differences of the histograms of Figure S27.

To confirm that the occurrence of multiple inequivalent ground states in Figure 3 is not an artifact of the PBE+D3(BJ) level of theory adopted here, and more specifically, to confirm that the distinction between the high-energy structures and the low-energy structures also holds for other levels of theory, the energy differences between 10 of the optimized structures of the γ, δ_{Cs}, and δ_{FA} phases shown in Figure 3 are recalculated with different XC functionals and with RPA+HF, as reported in Section 6 of the SI. Depending on the level of theory, both the energy spread within a group as well as the energy gap separating the two groups vary. However, besides one exception, the low-energy structures remain more stable than

https://doi.org/10.1021/acs.chemmater.2c01508
Chem. Mater. 2022, 34, 8561−8576

the high-energy structures. Moreover, using different XC functionals to perform the optimization leads to approximately the same energy differences between the phases, as discussed in Section 7 in the SI. Therefore, we can assume that the structures with the lowest PBE+D3(BJ) energy for each phase are adequate structures to calculate the ground state energy differences between the phases also for all other levels of theory. Furthermore, as discussed in Section 8 of the SI, similar observations arise when generating initial configurations by randomly displacing atoms in the structure rather than extracting them from a *prior* MD run and subsequently optimizing these resulting structures. These observations also confirm the robustness of this unexpected observation with respect to the chosen level of theory. As we will show later, the here revealed energy difference between the high- and low-energy structures has a profound effect on the predicted transition temperature.

4.1.2. Effect of XC Functionals and Dispersion Method on the Ground State Energy. The second step when determining the ground state energy is to assess the accuracy of the XC functionals on the ground state energy differences between the phases. As mentioned before, the RPA+HF results are adopted as the most accurate estimate and hence are the reference for our comparison, given that a comparison of the calculated results with experimental ones is necessarily postponed to Section 4.3, as this also requires the vibrational free energy. To guide the discussion, we introduce the following terminology to compare energy differences between different phases and levels of theory (LOT). First, the metric $\Delta_{\text{phase}_1-\text{phase}_2}E^{\text{LOT}}$ denotes, for a fixed level of theory, the energy difference between two phases. Subsequently, to compare how different XC functionals are able to reproduce this energy difference when calculated using RPA+HF, we will focus on the metric $\Delta^{\text{LOT}_1-\text{LOT}_2}\Delta_{\text{phase}_1-\text{phase}_2}E$, which is the difference between $\Delta_{\text{phase}_1-\text{phase}_2}E^{\text{LOT}_1}$ and $\Delta_{\text{phase}_1-\text{phase}_2}E^{\text{LOT}_2}$, calculated between two different levels of theory, one of which will be RPA+HF.

Figure 4 summarizes, for each functional and dispersion method, the ground state energy differences between the δ_{Cs} and the γ phase on the one hand (purple, $\Delta_{\delta_{\text{Cs}}-\gamma}E$) and the δ_{FA} and the γ phase on the other hand (green, $\Delta_{\delta_{\text{FA}}-\gamma}E$). These differences are visualized with respect to the RPA+HF results (dotted lines, $\Delta_{\delta-\gamma}E^{\text{RPA+HF}}$), which equals −12.7 kJ/mol for the δ_{Cs} phase and 0.35 kJ/mol for the δ_{FA} phase. The sizes of the different bars indicate the metric $\Delta^{\text{XC}-(\text{RPA+HF})}\Delta_{\delta-\gamma}E$ defined above; the smaller this bar, the better the XC functional reproduces the RPA+HF result. Figure 4 demonstrates that the PBE+D3(BJ), PBE+MBD/FI, and SCAN+rVV10 functionals show the best agreement with RPA+HF, because they lead to the lowest absolute values for $\Delta^{\text{XC}-(\text{RPA+HF})}\Delta_{\delta_{\text{Cs}}-\gamma}E$ and $\Delta^{\text{XC}-(\text{RPA+HF})}\Delta_{\delta_{\text{FA}}-\gamma}E$.

When comparing the results for the XC functionals without dispersion corrections, the PBE and HSE06 results are very similar. However, they heavily overestimate $\Delta_{\delta_{\text{Cs}}-\gamma}E$. Those results are improved when using the M06-L, PBEsol, or SCAN functionals. However, the best results are obtained for the vdW-DF2 functional, which is a nonlocal XC functional that includes an approximation of the van der Waals interactions.[117]

For the investigated GGA, mGGA, and hybrid XC functionals, the inclusion of an appropriate dispersion method can almost completely correct the error of the energies computed without a dispersion method. Not all dispersion methods lead to satisfying results, however, and especially the D2, Tkatchenko−Scheffler (TS), and many-body dispersion (MBD) methods yield large deviations on the energy differences. The MBD method is known to perform poorly for ionic systems. The MBD/FI dispersion method of Gould et al. corrects the MBD method by incorporating ionic effects to describe the polarizability.[114] For $CsPbI_3$, which is an ionic system, this is necessary as the MBD error is corrected almost completely for the MBD/FI dispersion method. Inclusion of the Axilrod−Teller−Muto (ATM) contributions to the D3(BJ) dispersion barely changes the obtained results (approximately 0.3 kJ/mol).

To determine the electronic structure of $CsPbI_3$, it is important to include spin−orbit coupling (SOC).[52] However, as demonstrated for the PBE and HSE06 XC functionals in Figure 4, SOC has a small effect of about 0.4 kJ/mol on the ground state energy differences between the phases, because SOC mainly affects the neighborhood around the nuclei.[125] Therefore, the SOC effects on the energy are very similar for the three different phases and cancel out when calculating the energy differences between the phases.

As visualized in Figure S28, most XC functionals and dispersion methods predict energy differences between different structures of the same phase that are roughly the same as the RPA+HF results, with HSE06+D3(BJ), SCAN+rVV10, and PBE+D3(BJ) performing the best.

4.2. Thermal Corrections: The Vibrational Free Energy. *4.2.1. Validation of the Machine Learning Potentials.* Given our focus on determining a phase-transferable MLP, we first turn our attention to the MLP trained on the three different phases, MLP_{all}, when determining the thermal corrections to the ground state energy. MLP_{all} is shown to exhibit a mean absolute error (MAE) of 0.7 kJ/mol per formula unit on the energy and 29 meV/Å on the forces. Especially the latter value should be as low as possible, as only the forces are necessary to perform the MD calculations. The MAE on the forces for MLP_{all} is significantly lower than for the MLPs trained on $CsPbI_3$ by Jinnouchi et al., which obtained an error of approximately 70 meV/Å. This is not unexpected, given that our training set is approximately 100 times larger. Also, the MLPs trained by Chen and co-workers for $MAPbI_3$ have a significantly higher MAE on the forces.[96,98] A possible explanation is that their MLPs use the hyperbolic tangent as the activation function, as mentioned in their work, while SchNet uses the shifted softplus.[142]

While training the MLP on each phase individually reduces the phase-transferability of the model, it can also reduce the MAE on the forces for this specific phase. However, the MAE on the forces for MLP_{γ}, $\text{MLP}_{\delta_{\text{Cs}}}$, and $\text{MLP}_{\delta_{\text{FA}}}$ are 29 meV/Å, 17 meV/Å, and 27 meV/Å, respectively, which are only slightly smaller than or of the same magnitude as the errors obtained when using MLP_{all}. This indicates that it is possible to train one phase-transferable MLP for multiple $CsPbI_3$ phases without a significant loss of accuracy. Moreover, Section 4.2 of the SI discusses the effect of the data set size on these errors. When training an MLP on a specific phase, using all generated *ab initio* data decreases the MAE on the forces. When training on all phases simultaneously (i.e., MLP_{all}) instead, the best MAE is approximately achieved already when considering only about a fourth of the total generated data for each phase. This indicates that learning the interactions of one phase can help

https://doi.org/10.1021/acs.chemmater.2c01508
Chem. Mater. 2022, 34, 8561−8576

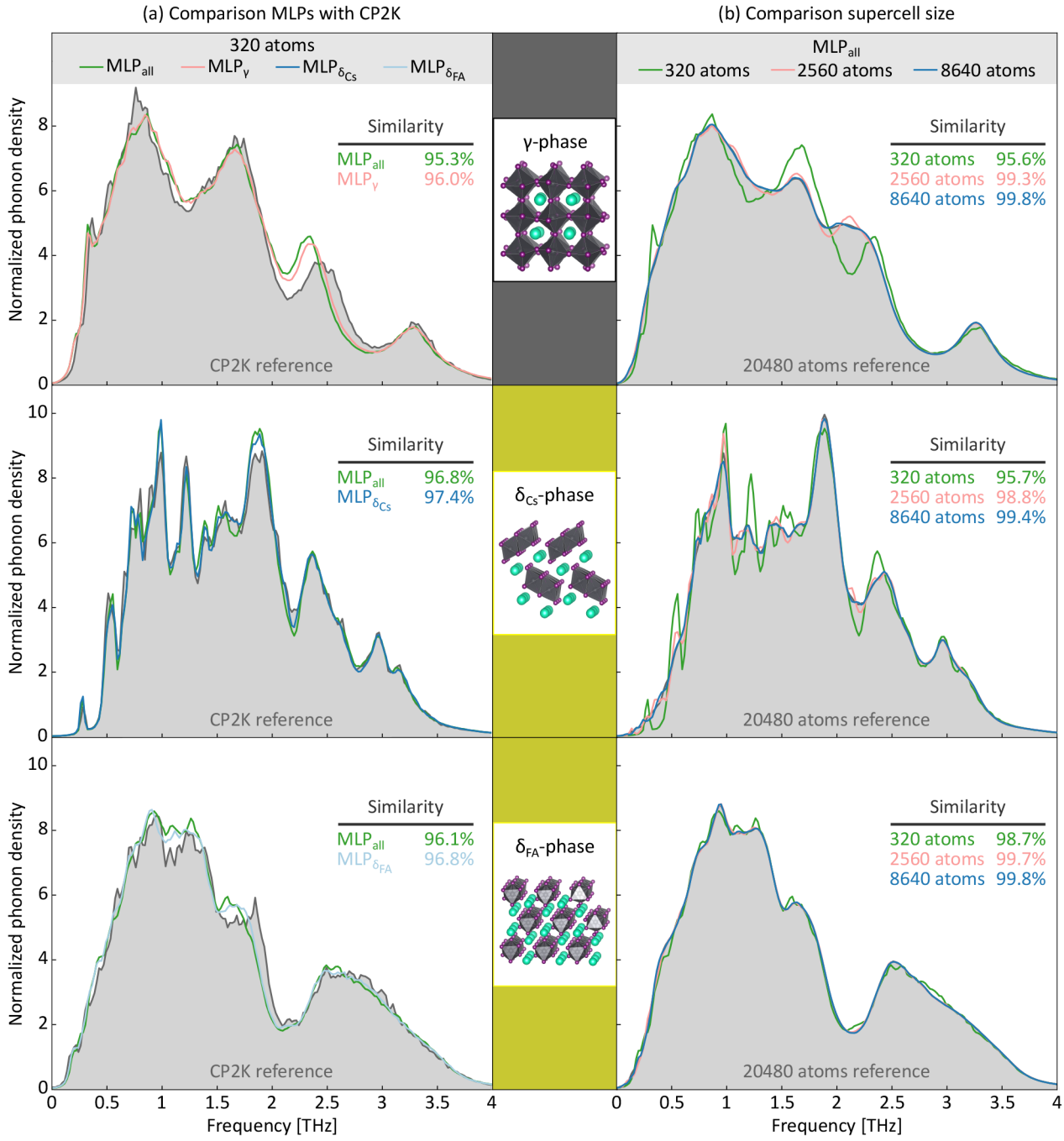

Figure 5. Vibrational density of states at 300 K for the γ, δ_{Cs}, and δ_{FA} phases. (a) Comparison of the VDOS obtained with the different MLPs with the CP2K results. (b) Comparison of the VDOS for different supercell sizes. For all VDOS, the similarity (defined with eq 4.1) with the corresponding reference VDOS is quantified.

learning the interactions for another phase; i.e., there is a clear transferability between the interactions of the different phases.

These are very promising results for further phase stability and phase transition studies, as a proper description of a phase transition requires a single MLP that can describe both phases simultaneously. It remains to be investigated in future studies how much additional training data would be necessary to also simulate the phase transitions with an MLP, in addition to the relative phase stabilities of interest here. This aspect is beyond the scope of the current paper. In any case, the current results suggest that it is possible to train an MLP to determine phase stabilities if sufficient high-quality training data is provided. Moreover, when only simulating distinct (meta)stable regions of the phase space, the total number of MLPs that have to be trained can be reduced while requiring significantly less input data, and this is at the expense of only a small increase of the MAE on the forces.

4.2.2. Determining the Vibrational Density of States. Figure 5a compares the VDOS at 300 K obtained using the different MLPs with the VDOS obtained using CP2K, for all three phases. The similarity between the normalized VDOS $\left(\frac{D(\nu)}{N_f}\right)$ and the corresponding normalized reference VDOS

https://doi.org/10.1021/acs.chemmater.2c01508
Chem. Mater. 2022, 34, 8561−8576

$\left(\frac{D_{ref}(\nu)}{N_{f,ref}}\right)$ is defined here as the difference inthe total number of modes that are found at a given frequency and is calculated with the following formula:

$$\text{Similarity} = \left[1 - \frac{\int_0^\infty d\nu \left|\frac{D(\nu)}{N_f} - \frac{D_{ref}(\nu)}{N_{f,ref}}\right|}{2}\right] \times 100\% \quad (4.1)$$

With this definition, the spectra are the same when the similarity is 100% and have no overlap when the similarity is 0%. All MLPs resemble the CP2K results rather closely with a similarity exceeding 95%. Moreover, the similarity between the VDOS obtained with CP2K and that obtained with the MLPs is of the same order of magnitude as the similarity between the VDOS obtained with different CP2K MD runs, shown in Figure S35. This slight dissimilarity between CP2K runs is the result of noise on the spectra, stemming from the short length of the CP2K MD runs of 24 ps. This issue does not occur for the MLPs, because the computational efficiency of these MLPs allows for substantially longer calculations (see also Section 10.1 in the SI).

The most remarkable difference between the VDOS calculated with an MLP and the one calculated with CP2K is found for the γ phase, for which the peak at 2.5 THz is slightly shifted for both MLP_γ and MLP_{all}. Section 12 of the SI visualizes the partial VDOS of the γ phase at 300 K for each element, calculated with CP2K and with MLP_{all}. It demonstrates that the peak at 2.5 THz is constructed by modes involving the Pb^{2+} and I^- ions. The shift of the 2.5 THz peak for MLP_{all} mainly originates from the iodine VDOS which we hypothesize to stem from a suboptimal MLP reproducibility of the Pb−I−Pb bond angle movements, because SchNet only uses distances to model interactions between atoms.[142] It might be interesting for future work to also investigate other MLP frameworks which employ different atomic representations. Overall, however, the large similarity index validates the application of the MLPs to calculate the VDOS for each of the phases and to determine thermal corrections on the ground state energy.

Comparing our results with previous works reveals that the PBE VDOS for the γ phase of $CsPbI_3$ reported by Kaiser et al.[67] is very similar to our calculated VDOS with CP2K at 400 and 500 K, which are reported in Section 10.2 of the SI. Comparing the VDOS of Gu et al. with the VDOS of Figure 5 also shows an overall resemblance.[66] However, on average more peaks are present in their calculations, possibly due to the smaller supercell sizes that they used.

When investigating the MLPs trained on each of the different phases, MLP_γ gives only a marginal improvement compared to MLP_{all}, in line with the similar errors found when training the different MLPs. Also, the VDOS for the δ_{Cs} and δ_{FA} phases obtained with MLP_{all} are practically the same as the VDOS obtained with the $MLP_{\delta_{Cs}}$ and $MLP_{\delta_{FA}}$, respectively. This is an extra validation of our goal to train one MLP for all phases. Given these results, MLP_{all} is adopted to calculate the thermal corrections in the rest of this work.

As visualized in Figure 5b, the effect of the supercell size on the VDOS is of the same order of magnitude as the effect of introducing an MLP for the γ and δ_{Cs} phases compared to the CP2K VDOS. The main difference is that the dissimilarity between the VDOS using different supercells cannot be ascribed to random noise because the MLP MD runs are fully converged. As a result, these dissimilarities completely originate from the different sizes of the supercell. The VDOS obtained with 8640 atoms and 20 480 atoms are practically the same (similarity index > 99%). Given that a 2560-atom supercell almost completely corrects for the error made with 320 atoms (similarity index > 98%), supercells of 2560 atoms are used for each phase to obtain the free energy as a function of temperature, as reported in Section 4.3.

Besides retaining the small shift for the 2.5 THz peak of the γ phase compared to the CP2K results, using bigger supercells mainly smoothens most peaks of the smallest supercell cell, sometimes removing the peak completely. For example, the two peaks around 0.5 THz for the 320-atom supercell of the δ_{Cs} phase get flattened when using a supercell of at least 2560 atoms. This may result from modes that occur on length scales that are too large to be described in the 320-atoms supercell but which do fit in a 2560-atom supercell. Because of eq 2.5, the absence of these modes in the 320-atom supercell will artificially promote the modes that do fit in this small supercell, which creates more distinct peaks.

Despite the differences in the VDOS for different sizes of the supercell, these differences are of lesser importance for the vibrational free energy, which averages over the whole frequency range through eq 2.2. As a result, the differences between the VDOS observed in Figure 5 lead to only small changes in vibrational free energy (see Figure 6), as discussed in more detail in Section 13 of the SI. Thus, if one is only interested in obtaining thermal corrections to the free energy, it might be sufficient to calculate the VDOS using CP2K on smaller unit cells. However, care should be exerted how these errors in the VDOS, introduced when using too small supercells, may impact other properties or other materials.[69]

4.3. Helmholtz Free Energy and Final Phase Transition Temperature. The calculations of Sections 4.1 and 4.2 are necessary to determine the total Helmholtz free energy as a function of temperature and, hence, to predict the temperature at which $CsPbI_3$ transitions to its δ_{Cs} phase. Besides the VDOS at 300 K reported in Figure 5, the VDOS for all phases are also calculated at all other temperatures between 100 and 600 K, with steps of 100 K (see Section 10.2 in the SI). From the VDOS, the vibrational free energy is calculated via eq 2.2, which is then added to the ground state energy to obtain the total Helmholtz free energy at that temperature. This yields $\Delta_{\delta-\gamma}F(T) = \Delta_{\delta-\gamma}E_{GS}^{LOT_1} + \Delta_{\delta-\gamma}F_{vib}^{LOT_2}(T)$. The different levels of theory considered for the ground state energy are reported in Figure 4 with RPA+HF as the reference method. For the vibrational free energy, the different levels of theory are reported in Figure 5, using the MLP on a 2560-atom unit cell as the reference.

Figure 6 visualizes the difference in total free energy as a function of temperature, again using the γ phase as the reference phase ($\Delta_{\delta_{Cs}-\gamma}F(T)$ in purple and $\Delta_{\delta_{FA}-\gamma}F(T)$ in green). The figure reveals that the δ_{FA} phase is never the most stable phase for $CsPbI_3$, as expected given the absence of any experimental evidence for this phase in the material. Furthermore, Figure 6 indicates that the γ phase is the most stable phase at temperatures above 500 K, while it transitions to the δ_{Cs} phase for lower temperatures. This is in satisfactory agreement with the experimental results depicted in Figure 1. For instance, Dastidar et al. predicted the transition to occur at slightly higher temperatures of 548 to 599 K.[24] They also

https://doi.org/10.1021/acs.chemmater.2c01508
Chem. Mater. 2022, 34, 8561−8576

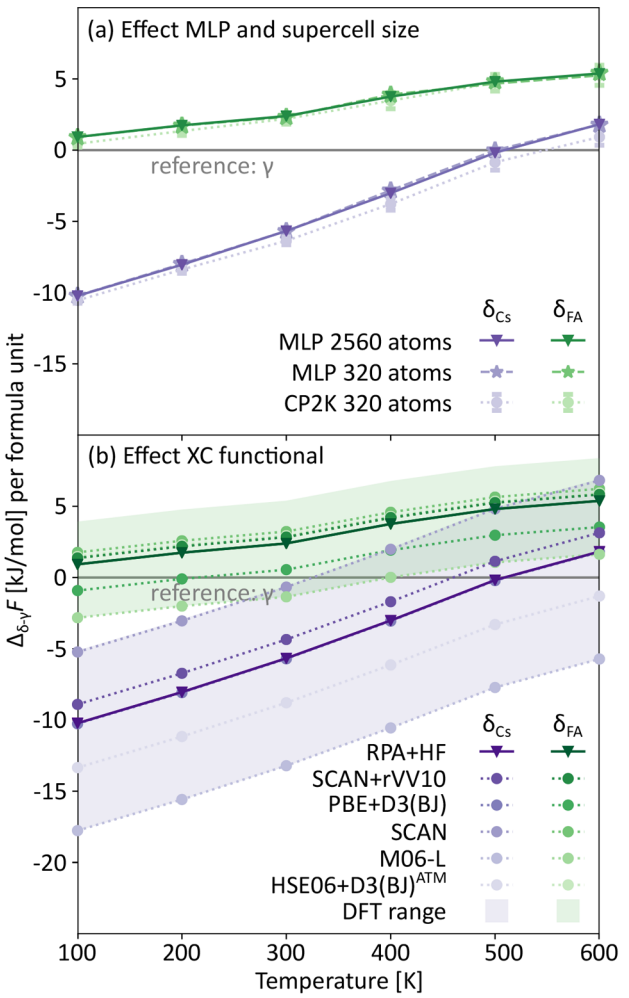

Figure 6. Total free energy difference of the δ_{Cs} (purple, $\Delta_{\delta_{Cs}-\gamma}F(T)$) and δ_{FA} (green, $\Delta_{\delta_{FA}-\gamma}F(T)$) phases with respect to the γ phase as a function of temperature. In both panels, the reference values are displayed with top-down triangles. (a) Comparison of the effect of using CP2K or an MLP (on either a 320-atom or a 2560-atom supercell) to calculate $\Delta_{\delta-\gamma}F_{vib}(T)$, in all cases obtained starting from $\Delta_{\delta-\gamma}E_{GS}^{RPA+HF}$. For the CP2K calculations, a small standard deviation is visible, which stems from the noise on the VDOS because the MD trajectories are only 24 ps long. The MLP trajectories are 40 times longer and, therefore, the error bar is not visible. (b) Comparison of the impact of different XC functionals to calculate $\Delta_{\delta-\gamma}E_{GS}$, using in all cases $\Delta_{\delta-\gamma}F_{vib}^{MLP,2560}(T)$ to account for thermal corrections. The shaded area shows the complete range of results using the XC functionals of Figure 4, excluding the PBE, PBE+D2, PBE+MBD, PBE+TS, and HSE06 XC functionals, which were identified before as clear outliers.

reported the change in enthalpy at the transition temperature to be around 13.7 to 15.1 kJ/mol,[24] which coincides well with the results of Steele et al.[28] The calculated ground state energy difference between the γ and the δ_{Cs} phases with RPA+HF, 12.7 kJ/mol, is in good agreement with the measured enthalpy difference by Dastidar and co-workers.[24] This experimental validation of the RPA+HF results justifies its use as the reference method for the XC functionals and dispersion methods in this work.

As displayed in Figure 6a, the size of the supercell has a negligible effect on the free energy differences. Applying the MLP instead of CP2K calculations has a bigger effect, although the effect remains small. Using CP2K slightly improves the prediction of the transition temperature to approximately 550 K. In contrast, Figure 6b indicates that the choice of XC functional to calculate the ground state energy substantially affects the transition temperature prediction. Using the right XC functional and dispersion method is hence of paramount importance to get the transition temperature right. For example, the SCAN functional predicts a transition temperature around 320 K, while the M06-L functional does not predict a transition below 600 K.

The sensitivity of the transition temperature on the ground state energy results from the slow and approximately linear decrease of $\Delta_{\delta_{Cs}-\gamma}F(T)$ as a function of temperature. The free energy difference decreases on average by 2.5 kJ/mol per increase in temperature of 100 K. Therefore, the prior optimization of the ground state structure is important, as discussed in Section 4.1, as it is possible to get stuck in a local minimum which is almost 4 kJ/mol higher than the global minima. This would shift the transition temperature *circa* 160 K. The primary importance of the electronic structure method on the free energy was also observed for phase stabilities in metal−organic frameworks by Wieme et al.[58]

While spin−orbit coupling is not included in the RPA+HF calculations, it only changes the ground state energy differences with 0.7 kJ/mol or less. This would correspond with an estimated change in transition temperature of only 30 K, which is substantially smaller than the other potential origins of inaccuracy discussed here.

5. CONCLUSIONS

In this work, we have proposed and validated a computational methodology to accurately determine the Helmholtz free energy as a function of temperature for the γ, δ_{Cs}, and δ_{FA} phases of $CsPbI_3$. These calculations are performed with the goal to retrieve the experimentally measured transition temperature of the γ-to-δ_{Cs} phase transition of $CsPbI_3$, which, if successful, would validate the applicability of this methodology to predict the phase transition temperature in similar materials and understand different phase-stabilizing effects. The calculation of the Helmholtz free energy consists of two parts, the ground state energy at 0 K and the vibrational free energy at a range of temperatures encompassing the expected phase transition temperature.

To obtain reference results for the ground state energy, highly accurate but computationally expensive RPA+HF calculations were performed, yielding an energy difference of 12.7 kJ/mol per formula unit between the γ and the δ_{Cs} phases. This result was used to benchmark the accuracy of several computationally less expensive XC functionals and dispersion methods. We observed that including a suitable dispersion method was necessary to reproduce the RPA+HF results. The best results were obtained with the PBE+D3(BJ), PBE+MBD/FI, and SCAN+rVV10 XC functionals, with a clear sensitivity of the transition temperature on the chosen XC functional. Depending on the specific choice of dispersion method or XC functional, the transition temperature was found to easily deviate from the reference value by several hundreds of Kelvin. In addition, we observed that these results were also very sensitive to the optimized structure chosen to calculate the ground state energy. We demonstrated that the optimization algorithm for the γ phase of $CsPbI_3$ could get stuck in a local

https://doi.org/10.1021/acs.chemmater.2c01508
Chem. Mater. 2022, 34, 8561−8576

minimum, with an energy of 4 kJ/mol per formula unit higher than the energy of the global minimum. This would artificially increase the transition temperature by approximately 160 K. Finally, the effect of the spin−orbit coupling interaction on the transition temperature was estimated to be smaller than 30 K.

To incorporate anharmonic effects in the vibrational free energy, the vibrational density of states was determined, which required long MD trajectories for large supercells to ensure convergence. To perform these long MD simulations, an MLP was trained. With the MLP, we could converge the VDOS for the length of the MD simulation and the supercell size. An 8640-atom supercell was necessary to converge the VDOS, although a 2560-atom supercell almost completely corrected the error made with the 320-atom supercell. For the 320-atom supercell, the error introduced due to the MLP with respect to the *ab initio* VDOS was similar to the error due to the smaller supercell size.

The total free energy differences between the $CsPbI_3$ phases change slowly as a function of temperature, making this the ideal benchmark system for our methodology and stipulating the need for highly accurate calculations to determine the transition temperature. By combining our ground state energies calculated at the highly accurate RPA+HF level with the vibrational free energy obtained with the phase-transferable MLP on a 2560-atom supercell, our approach predicted the transition temperature to be 500 K, which is only 50 to 100 K lower than measured experimentally. In contrast with the results for the VDOS, we demonstrated that the supercell size has a negligible effect on the vibrational free energy and transition temperature for $CsPbI_3$, while the MLP did cause a noticeable downward shift of roughly 50 K in the transition temperature. Because the error introduced when reducing the supercell size to 320 atoms or when shortening the MD simulations is small, the transition temperature predicted using *ab initio* calculations agrees unexpectedly well with experiment. One could conclude that it is therefore not necessarily important to train an MLP for performing long length and time scale simulations for predicting the transition temperature. However, given that our methodology already improved on the *ab initio* ground state energy differences between the various phases, one can expect an even more substantial improvement when considering larger spatiotemporal windows, for instance, when investigating the exact phase transition mechanism or when elucidating the effect of nanosizing on the phase stability of these materials.

The methodology established in this paper, which was critically validated for $CsPbI_3$, shows great potential to obtain insight in the phase stability and transition temperatures of other more complicated organic−inorganic MHPs such as $MAPbI_3$ and $FAPbI_3$, of course taking into account the intricacies introduced when simulating organic cations. Controlling the phase stability of MHPs remains a major challenge, and the opportunity to accurately calculate the Helmholtz free energy is therefore a very useful tool to gain insight in this challenge. Specifically, the here validated methodology can be adopted to evaluate the effect of different stabilizing factors put forward in literature, such as surface functionalization, doping, and strain engineering, on the phase stability of these materials without the need to account for possible confounding effects occurring during an experimental measurement. Therefore, the here proposed accurate yet computationally feasible procedure may prove to be a valuable tool to predict, understand, and design polymorphic behavior in MHPs with the goal to eventually bring these promising materials to practical and large-scale applications.

■ ASSOCIATED CONTENT

Supporting Information

The Supporting Information is available free of charge at https://pubs.acs.org/doi/10.1021/acs.chemmater.2c01508.

Flowchart to calculate the total Helmholtz free energy, further computational details for the VASP and CP2K calculations, MLP training and validation, histograms of the 101 optimized structures, effect of the XC functional on the ground state energy differences between the structures of the same phase and the structure optimization, creating new initial structures for the optimizations by randomly displacing the atoms, procedure to remove near-zero frequencies of the vibrational density of states, effect of the computational details on the vibrational density of states, averaging over multiple vibrational density of states obtained from CP2K MD runs, partial vibrational density of states, and analysis of the deviations in the vibrational density of states (PDF)

■ AUTHOR INFORMATION

Corresponding Authors

Sven M. J. Rogge − *Center for Molecular Modeling (CMM), Ghent University, 9052 Zwijnaarde, Belgium;* orcid.org/0000-0003-4493-5708; Email: sven.rogge@ugent.be

Veronique Van Speybroeck − *Center for Molecular Modeling (CMM), Ghent University, 9052 Zwijnaarde, Belgium;* orcid.org/0000-0003-2206-178X; Email: veronique.vanspeybroeck@ugent.be

Authors

Tom Braeckevelt − *Center for Molecular Modeling (CMM), Ghent University, 9052 Zwijnaarde, Belgium; Department of Chemistry, KU Leuven, Leuven 3001, Belgium*

Ruben Goeminne − *Center for Molecular Modeling (CMM), Ghent University, 9052 Zwijnaarde, Belgium*

Sander Vandenhaute − *Center for Molecular Modeling (CMM), Ghent University, 9052 Zwijnaarde, Belgium*

Sander Borgmans − *Center for Molecular Modeling (CMM), Ghent University, 9052 Zwijnaarde, Belgium*

Toon Verstraelen − *Center for Molecular Modeling (CMM), Ghent University, 9052 Zwijnaarde, Belgium;* orcid.org/0000-0001-9288-5608

Julian A. Steele − *cMACS, Department of Microbial and Molecular Systems, KU Leuven, Leuven 3001, Belgium; School of Mathematics and Physics, The University of Queensland, Brisbane, Queensland 4072, Australia;* orcid.org/0000-0001-7982-4413

Maarten B. J. Roeffaers − *cMACS, Department of Microbial and Molecular Systems, KU Leuven, Leuven 3001, Belgium;* orcid.org/0000-0001-6582-6514

Johan Hofkens − *Department of Chemistry, KU Leuven, Leuven 3001, Belgium; Max Plank Institute for Polymer Research, D-55128 Mainz, Germany;* orcid.org/0000-0002-9101-0567

Complete contact information is available at: https://pubs.acs.org/10.1021/acs.chemmater.2c01508

https://doi.org/10.1021/acs.chemmater.2c01508
Chem. Mater. 2022, 34, 8561−8576

Notes

The authors declare no competing financial interest.
Data is available at 10.5281/zenodo.6807899.

■ ACKNOWLEDGMENTS

The authors gratefully acknowledge financial support from the Research Foundation—Flanders (FWO Grant Nos. 1SC1319N, 11H6821N, 12T3522N, G.0B39.15, G.0B49.15, G098319N, 1280021N, 12Y7221N, 12Y6418N, 1242922N, V400622N, VS052320N, and ZW15_09-GOH6316N), the Research Fund of Ghent University (iBOF-21-085 PERSIST), the KU Leuven Research Fund (C14/19/079, iBOF-21-085 PERSIST), the KU Leuven Industrial Research Fund (C3/19/046), the Flemish government through long term structural funding Methusalem (CASAS2, Meth/15/04). and the MPI to J.H. as an MPI fellow. T.V. and V.V.S. furthermore acknowledge the Research Fund of Ghent University (BOF) for its financial support. The computational resources and services used in this work were provided by VSC (Flemish Supercomputer Center), funded by the Research Foundation—Flanders (FWO), and the Flemish Government.

■ REFERENCES

(1) Kim, J. Y.; Lee, J.-W.; Jung, H. S.; Shin, H.; Park, N.-G. High-Efficiency Perovskite Solar Cells. *Chem. Rev.* **2020**, *120*, 7867−7918.
(2) Zhang, K.; Zhu, N.; Zhang, M.; Wang, L.; Xing, J. Opportunities and challenges in perovskite LED commercialization. *J. Mater. Chem. C* **2021**, *9*, 3795−3799.
(3) Kim, Y. C.; Kim, K. H.; Son, D.-Y.; Jeong, D.-N.; Seo, J.-Y.; Choi, Y. S.; Han, I. T.; Lee, S. Y.; Park, N.-G. Printable organometallic perovskite enables large-area, low-dose X-ray imaging. *Nature* **2017**, *550*, 87−91.
(4) Zhang, W.; Eperon, G. E.; Snaith, H. J. Metal halide perovskites for energy applications. *Nat. Energy* **2016**, *1*, 16048.
(5) Sutherland, B. R.; Sargent, E. H. Perovskite photonic sources. *Nat. Photonics* **2016**, *10*, 295−302.
(6) Manser, J. S.; Christians, J. A.; Kamat, P. V. Intriguing Optoelectronic Properties of Metal Halide Perovskites. *Chem. Rev.* **2016**, *116*, 12956−13008.
(7) Chouhan, L.; Ghimire, S.; Subrahmanyam, C.; Miyasaka, T.; Biju, V. Synthesis, optoelectronic properties and applications of halide perovskites. *Chem. Soc. Rev.* **2020**, *49*, 2869−2885.
(8) Kojima, A.; Teshima, K.; Shirai, Y.; Miyasaka, T. Organometal Halide Perovskites as Visible-Light Sensitizers for Photovoltaic Cells. *J. Am. Chem. Soc.* **2009**, *131*, 6050−6051.
(9) Kim, H.-S.; Lee, C.-R.; Im, J.-H.; Lee, K.-B.; Moehl, T.; Marchioro, A.; Moon, S.-J.; Humphry-Baker, R.; Yum, J.-H.; Moser, J. E.; Grätzel, M.; Park, N.-G. Lead Iodide Perovskite Sensitized All-Solid-State Submicron Thin Film Mesoscopic Solar Cell with Efficiency Exceeding 9%. *Sci. Rep.* **2012**, *2*, 591.
(10) Lee, J.-W.; Seol, D.-J.; Cho, A.-N.; Park, N.-G. High-Efficiency Perovskite Solar Cells Based on the Black Polymorph of $HC(NH_2)_2PbI_3$. *Adv. Mater.* **2014**, *26*, 4991−4998.
(11) Eperon, G. E.; Stranks, S. D.; Menelaou, C.; Johnston, M. B.; Herz, L. M.; Snaith, H. J. Formamidinium lead trihalide: a broadly tunable perovskite for efficient planar heterojunction solar cells. *Energy Environ. Sci.* **2014**, *7*, 982−988.
(12) Ganose, A. M.; Savory, C. N.; Scanlon, D. O. Beyond methylammonium lead iodide: prospects for the emergent field of ns^2 containing solar absorbers. *Chem. Commun.* **2017**, *53*, 20−44.
(13) Sun, Q.; Yin, W.-J.; Wei, S.-H. Searching for stable perovskite solar cell materials using materials genome techniques and high-throughput calculations. *J. Mater. Chem. C* **2020**, *8*, 12012−12035.
(14) Schade, L.; Wright, A. D.; Johnson, R. D.; Dollmann, M.; Wenger, B.; Nayak, P. K.; Prabhakaran, D.; Herz, L. M.; Nicholas, R.; Snaith, H. J.; Radaelli, P. G. Structural and Optical Properties of $Cs_2AgBiBr_6$ Double Perovskite. *ACS Energy Lett.* **2019**, *4*, 299−305.
(15) Keshavarz, M.; Debroye, E.; Ottesen, M.; Martin, C.; Zhang, H.; Fron, E.; Küchler, R.; Steele, J. A.; Bremholm, M.; Van de Vondel, J.; Wang, H. I.; Bonn, M.; Roeffaers, M. B. J.; Wiedmann, S.; Hofkens, J. Tuning the Structural and Optoelectronic Properties of $Cs_2AgBiBr_6$ Double-Perovskite Single Crystals through Alkali-Metal Substitution. *Adv. Mater.* **2020**, *32*, 2001878.
(16) Gao, X.; Zhang, X.; Yin, W.; Wang, H.; Hu, Y.; Zhang, Q.; Shi, Z.; Colvin, V. L.; Yu, W. W.; Zhang, Y. Ruddlesden−Popper Perovskites: Synthesis and Optical Properties for Optoelectronic Applications. *Adv. Sci.* **2019**, *6*, 1900941.
(17) Zheng, Y.; Niu, T.; Ran, X.; Qiu, J.; Li, B.; Xia, Y.; Chen, Y.; Huang, W. Unique characteristics of 2D Ruddlesden−Popper (2DRP) perovskite for future photovoltaic application. *J. Mater. Chem. A* **2019**, *7*, 13860−13872.
(18) Liang, C.; Gu, H.; Xia, Y.; Wang, Z.; Liu, X.; Xia, J.; Zuo, S.; Hu, Y.; Gao, X.; Hui, W.; Chao, L.; Niu, T.; Fang, M.; Lu, H.; Dong, H.; Yu, H.; Chen, S.; Ran, X.; Song, L.; Li, B.; Zhang, J.; Peng, Y.; Shao, G.; Wang, J.; Chen, Y.; Xing, G.; Huang, W. Two-dimensional Ruddlesden−Popper layered perovskite solar cells based on phase-pure thin films. *Nat. Energy* **2021**, *6*, 38−45.
(19) Yang, J.; Siempelkamp, B. D.; Liu, D.; Kelly, T. L. Investigation of $CH_3NH_3PbI_3$ Degradation Rates and Mechanisms in Controlled Humidity Environments Using in Situ Techniques. *ACS Nano* **2015**, *9*, 1955−1963.
(20) Wang, R.; Mujahid, M.; Duan, Y.; Wang, Z.-K.; Xue, J.; Yang, Y. A Review of Perovskites Solar Cell Stability. *Adv. Funct. Mater.* **2019**, *29*, 1808843.
(21) Christians, J. A.; Miranda Herrera, P. A.; Kamat, P. V. Transformation of the Excited State and Photovoltaic Efficiency of $CH_3NH_3PbI_3$ Perovskite upon Controlled Exposure to Humidified Air. *J. Am. Chem. Soc.* **2015**, *137*, 1530−1538.
(22) Stoumpos, C. C.; Malliakas, C. D.; Kanatzidis, M. G. Semiconducting Tin and Lead Iodide Perovskites with Organic Cations: Phase Transitions, High Mobilities, and Near-Infrared Photoluminescent Properties. *Inorg.* **2013**, *52*, 9019−9038.
(23) Binek, A.; Hanusch, F. C.; Docampo, P.; Bein, T. Stabilization of the Trigonal High-Temperature Phase of Formamidinium Lead Iodide. *J. Phys. Chem. Lett.* **2015**, *6*, 1249−1253.
(24) Dastidar, S.; Hawley, C. J.; Dillon, A. D.; Gutierrez-Perez, A. D.; Spanier, J. E.; Fafarman, A. T. Quantitative Phase-Change Thermodynamics and Metastability of Perovskite-Phase Cesium Lead Iodide. *J. Phys. Chem. Lett.* **2017**, *8*, 1278−1282.
(25) Sutton, R. J.; Filip, M. R.; Haghighirad, A. A.; Sakai, N.; Wenger, B.; Giustino, F.; Snaith, H. J. Cubic or Orthorhombic? Revealing the Crystal Structure of Metastable Black-Phase $CsPbI_3$ by Theory and Experiment. *ACS Energy Lett.* **2018**, *3*, 1787−1794.
(26) Marronnier, A.; Roma, G.; Boyer-Richard, S.; Pedesseau, L.; Jancu, J.-M.; Bonnassieux, Y.; Katan, C.; Stoumpos, C. C.; Kanatzidis, M. G.; Even, J. Anharmonicity and Disorder in the Black Phases of Cesium Lead Iodide Used for Stable Inorganic Perovskite Solar Cells. *ACS Nano* **2018**, *12*, 3477−3486.
(27) Xiang, W.; Liu, S. F.; Tress, W. A review on the stability of inorganic metal halide perovskites: challenges and opportunities for stable solar cells. *Energy Environ. Sci.* **2021**, *14*, 2090−2113.
(28) Steele, J. A.; Jin, H.; Dovgaliuk, I.; Berger, R. F.; Braeckevelt, T.; Yuan, H.; Martin, C.; Solano, E.; Lejaeghere, K.; Rogge, S. M. J.; Notebaert, C.; Vandezande, W.; Janssen, K. P. F.; Goderis, B.; Debroye, E.; Wang, Y.-K.; Dong, Y.; Ma, D.; Saidaminov, M.; Tan, H.; Lu, Z.; Dyadkin, V.; Chernyshov, D.; Van Speybroeck, V.; Sargent, E. H.; Hofkens, J.; Roeffaers, M. B. J. Thermal unequilibrium of strained black $CsPbI_3$ thin films. *Science* **2019**, *365*, 679−684.
(29) Steele, J. A.; Solano, E.; Jin, H.; Prakasam, V.; Braeckevelt, T.; Yuan, H.; Lin, Z.; de Kloe, R.; Wang, Q.; Rogge, S. M. J.; Van Speybroeck, V.; Chernyshov, D.; Hofkens, J.; Roeffaers, M. B. J. Texture Formation in Polycrystalline Thin Films of All-Inorganic Lead Halide Perovskite. *Adv. Mater.* **2021**, *33*, 2007224.
(30) Chen, K.; Zhong, Q.; Chen, W.; Sang, B.; Wang, Y.; Yang, T.; Liu, Y.; Zhang, Y.; Zhang, H. Short-Chain Ligand-Passivated Stable α-

$CsPbI_3$ Quantum Dot for All-Inorganic Perovskite Solar Cells. *Adv. Funct. Mater.* **2019**, *29*, 1900991.
(31) Li, B.; Zhang, Y.; Fu, L.; Yu, T.; Zhou, S.; Zhang, L.; Yin, L. Surface passivation engineering strategy to fully-inorganic cubic $CsPbI_3$ perovskites for high-performance solar cells. *Nat. Commun.* **2018**, *9*, 1076.
(32) Li, F.; Pei, Y.; Xiao, F.; Zeng, T.; Yang, Z.; Xu, J.; Sun, J.; Peng, B.; Liu, M. Tailored dimensionality to regulate the phase stability of inorganic cesium lead iodide perovskites. *Nanoscale* **2018**, *10*, 6318−6322.
(33) Wu, T.; Wang, Y.; Dai, Z.; Cui, D.; Wang, T.; Meng, X.; Bi, E.; Yang, X.; Han, L. Efficient and Stable $CsPbI_3$ Solar Cells via Regulating Lattice Distortion with Surface Organic Terminal Groups. *Adv. Mater.* **2019**, *31*, 1900605.
(34) Dirin, D. N.; Protesescu, L.; Trummer, D.; Kochetygov, I. V.; Yakunin, S.; Krumeich, F.; Stadie, N. P.; Kovalenko, M. V. Harnessing Defect-Tolerance at the Nanoscale: Highly Luminescent Lead Halide Perovskite Nanocrystals in Mesoporous Silica Matrixes. *Nano Lett.* **2016**, *16*, 5866−5874.
(35) Lu, M.; Zhang, X.; Bai, X.; Wu, H.; Shen, X.; Zhang, Y.; Zhang, W.; Zheng, W.; Song, H.; Yu, W. W.; Rogach, A. L. Spontaneous Silver Doping and Surface Passivation of $CsPbI_3$ Perovskite Active Layer Enable Light-Emitting Devices with an External Quantum Efficiency of 11.2%. *ACS Energy Lett.* **2018**, *3*, 1571−1577.
(36) Eames, C.; Frost, J. M.; Barnes, P. R. F.; O'Regan, B. C.; Walsh, A.; Islam, M. S. Ionic transport in hybrid lead iodide perovskite solar cells. *Nat. Commun.* **2015**, *6*, 7497.
(37) Walsh, A. Principles of Chemical Bonding and Band Gap Engineering in Hybrid Organic−Inorganic Halide Perovskites. *J. Phys. Chem. C* **2015**, *119*, 5755−5760.
(38) da Silva, E. L.; Skelton, J. M.; Parker, S. C.; Walsh, A. Phase stability and transformations in the halide perovskite $CsSnI_3$. *Phys. Rev. B* **2015**, *91*, 144107.
(39) Kye, Y.-H.; Yu, C.-J.; Jong, U.-G.; Ri, K.-C.; Kim, J.-S.; Choe, S.-H.; Hong, S.-N.; Li, S.; Wilson, J. N.; Walsh, A. Vacancy-Driven Stabilization of the Cubic Perovskite Polymorph of $CsPbI_3$. *J. Phys. Chem. C* **2019**, *123*, 9735−9744.
(40) Jiang, J.; Liu, F.; Tranca, I.; Shen, Q.; Tao, S. Atomistic and Electronic Origin of Phase Instability of Metal Halide Perovskites. *ACS Appl. Energy Mater.* **2020**, *3*, 11548−11558.
(41) Marronnier, A.; Lee, H.; Geffroy, B.; Even, J.; Bonnassieux, Y.; Roma, G. Structural Instabilities Related to Highly Anharmonic Phonons in Halide Perovskites. *J. Phys. Chem. Lett.* **2017**, *8*, 2659−2665.
(42) Wang, B.; Novendra, N.; Navrotsky, A. Energetics, Structures, and Phase Transitions of Cubic and Orthorhombic Cesium Lead Iodide ($CsPbI_3$) Polymorphs. *J. Am. Chem. Soc.* **2019**, *141*, 14501−14504.
(43) An, Y.; Hidalgo, J.; Perini, C. A. R.; Castro-Méndez, A.-F.; Vagott, J. N.; Bairley, K.; Wang, S.; Li, X.; Correa-Baena, J.-P. Structural Stability of Formamidinium- and Cesium-Based Halide Perovskites. *ACS Energy Lett.* **2021**, *6*, 1942−1969.
(44) Han, Q.; Bae, S.-H.; Sun, P.; Hsieh, Y.-T.; Yang, Y. M.; Rim, Y. S.; Zhao, H.; Chen, Q.; Shi, W.; Li, G.; Yang, Y. Single Crystal Formamidinium Lead Iodide ($FAPbI_3$): Insight into the Structural, Optical, and Electrical Properties. *Adv. Mater.* **2016**, *28*, 2253−2258.
(45) Jeon, N. J.; Noh, J. H.; Yang, W. S.; Kim, Y. C.; Ryu, S.; Seo, J.; Seok, S. I. Compositional engineering of perovskite materials for high-performance solar cells. *Nature* **2015**, *517*, 476−480.
(46) Lejaeghere, K.; Bihlmayer, G.; Björkman, T.; Blaha, P.; Blügel, S.; Blum, V.; Caliste, D.; Castelli, I. E.; Clark, S. J.; Dal Corso, A. D.; de Gironcoli, S.; Deutsch, T.; Dewhurst, J. K.; Di Marco, I. D.; Draxl, C.; Dułak, M.; Eriksson, O.; Flores-Livas, J. A.; Garrity, K. F.; Genovese, L.; Giannozzi, P.; Giantomassi, M.; Goedecker, S.; Gonze, X.; Grånäs, O.; Gross, E. K. U.; Gulans, A.; Gygi, F.; Hamann, D. R.; Hasnip, P. J.; Holzwarth, N. A. W.; Iuşan, D.; Jochym, D. B.; Jollet, F.; Jones, D.; Kresse, G.; Koepernik, K.; Küçükbenli, E.; Kvashnin, Y. O.; Locht, I. L. M.; Lubeck, S.; Marsman, M.; Marzari, N.; Nitzsche, U.; Nordström, L.; Ozaki, T.; Paulatto, L.; Pickard, C. J.; Poelmans, W.; Probert, M. I. J.; Refson, K.; Richter, M.; Rignanese, G.-M.; Saha, S.; Scheffler, M.; Schlipf, M.; Schwarz, K.; Sharma, S.; Tavazza, F.; Thunström, P.; Tkatchenko, A.; Torrent, M.; Vanderbilt, D.; van Setten, M. J.; Van Speybroeck, V.; Wills, J. M.; Yates, J. R.; Zhang, G.-X.; Cottenier, S. Reproducibility in density functional theory calculations of solids. *Science* **2016**, *351*, aad3000.
(47) Lejaeghere, K.; Van Speybroeck, V.; Van Oost, G.; Cottenier, S. Error Estimates for Solid-State Density-Functional Theory Predictions: An Overview by Means of the Ground-State Elemental Crystals. *Crit. Rev. Solid State Mater. Sci.* **2014**, *39*, 1−24.
(48) Csonka, G. I.; Perdew, J. P.; Ruzsinszky, A.; Philipsen, P. H. T.; Lebègue, S.; Paier, J.; Vydrov, O. A.; Ángyán, J. G. Assessing the performance of recent density functionals for bulk solids. *Phys. Rev. B* **2009**, *79*, 155107.
(49) Goerigk, L.; Grimme, S. A thorough benchmark of density functional methods for general main group thermochemistry, kinetics, and noncovalent interactions. *Phys. Chem. Chem. Phys.* **2011**, *13*, 6670−6688.
(50) Grabowski, B.; Hickel, T.; Neugebauer, J. Ab initio study of the thermodynamic properties of nonmagnetic elementary fcc metals: Exchange-correlation-related error bars and chemical trends. *Phys. Rev. B* **2007**, *76*, 024309.
(51) Wiktor, J.; Röthlisberger, U.; Pasquarello, A. Predictive Determination of Band Gaps of Inorganic Halide Perovskites. *J. Phys. Chem. Lett.* **2017**, *8*, 5507−5512.
(52) Umari, P.; Mosconi, E.; De Angelis, F. Relativistic GW calculations on $CH_3NH_3PbI_3$ and $CH_3NH_3SnI_3$ Perovskites for Solar Cell Applications. *Sci. Rep.* **2015**, *4*, 4467.
(53) Brivio, F.; Butler, K. T.; Walsh, A.; van Schilfgaarde, M. Relativistic quasiparticle self-consistent electronic structure of hybrid halide perovskite photovoltaic absorbers. *Phys. Rev. B* **2014**, *89*, 155204.
(54) Filip, M. R.; Giustino, F. *GW* quasiparticle band gap of the hybrid organic-inorganic perovskite $CH_3NH_3PbI_3$: Effect of spin-orbit interaction, semicore electrons, and self-consistency. *Phys. Rev. B* **2014**, *90*, 245145.
(55) Gao, W.; Gao, X.; Abtew, T. A.; Sun, Y.-Y.; Zhang, S.; Zhang, P. Quasiparticle band gap of organic-inorganic hybrid perovskites: Crystal structure, spin-orbit coupling, and self-energy effects. *Phys. Rev. B* **2016**, *93*, 085202.
(56) Bokdam, M.; Lahnsteiner, J.; Ramberger, B.; Schäfer, T.; Kresse, G. Assessing Density Functionals Using Many Body Theory for Hybrid Perovskites. *Phys. Rev. Lett.* **2017**, *119*, 145501.
(57) Lahnsteiner, J.; Kresse, G.; Heinen, J.; Bokdam, M. Finite-temperature structure of the $MAPbI_3$ perovskite: Comparing density functional approximations and force fields to experiment. *Phys. Rev. Mater.* **2018**, *2*, 073604.
(58) Wieme, J.; Lejaeghere, K.; Kresse, G.; Van Speybroeck, V. Tuning the balance between dispersion and entropy to design temperature-responsive flexible metal-organic frameworks. *Nat. Commun.* **2018**, *9*, 4899.
(59) Ferreira, A. C.; Létoublon, A.; Paofai, S.; Raymond, S.; Ecolivet, C.; Rufflé, B.; Cordier, S.; Katan, C.; Saidaminov, M. I.; Zhumekenov, A. A.; Bakr, O. M.; Even, J.; Bourges, P. Elastic Softness of Hybrid Lead Halide Perovskites. *Phys. Rev. Lett.* **2018**, *121*, 085502.
(60) Altland, A.; Simons, B. D.*Condensed matter field theory*; Cambridge University Press: 2010.
(61) McQuarrie, D.*Quantum Chemistry*; University Science Books: 2008.
(62) Alfè, D. PHON: A program to calculate phonons using the small displacement method. *Comput. Phys. Commun.* **2009**, *180*, 2622−2633.
(63) Togo, A.; Tanaka, I. First principles phonon calculations in materials science. *Scr. Mater.* **2015**, *108*, 1−5.
(64) Peters, L. D. M.; Dietschreit, J. C. B.; Kussmann, J.; Ochsenfeld, C. Calculating free energies from the vibrational density of states function: Validation and critical assessment. *J. Chem. Phys.* **2019**, *150*, 194111.

https://doi.org/10.1021/acs.chemmater.2c01508
Chem. Mater. 2022, 34, 8561−8576

(65) Jong, U.-G.; Yu, C.-J.; Kye, Y.-H.; Kim, Y.-S.; Kim, C.-H.; Ri, S.-G. A first-principles study on the chemical stability of inorganic perovskite solid solutions $Cs_{1-x}Rb_xPbI_3$ at finite temperature and pressure. *J. Mater. Chem. A* **2018**, *6*, 17994−18002.
(66) Gu, H.-Y.; Yin, W.-J.; Gong, X.-G. Significant phonon anharmonicity drives phase transitions in $CsPbI_3$. *Appl. Phys. Lett.* **2021**, *119*, 191101.
(67) Kaiser, W.; Carignano, M.; Alothman, A. A.; Mosconi, E.; Kachmar, A.; Goddard, W. A.; De Angelis, F. First-Principles Molecular Dynamics in Metal-Halide Perovskites: Contrasting Generalized Gradient Approximation and Hybrid Functionals. *J. Phys. Chem. Lett.* **2021**, *12*, 11886−11893.
(68) Zhang, D.-B.; Sun, T.; Wentzcovitch, R. M. Phonon Quasiparticles and Anharmonic Free Energy in Complex Systems. *Phys. Rev. Lett.* **2014**, *112*, 058501.
(69) Lahnsteiner, J.; Bokdam, M. Anharmonic lattice dynamics in large thermodynamic ensembles with machine-learning force fields: $CsPbBr_3$, a phonon liquid with Cs rattlers. *Phys. Rev. B* **2022**, *105*, 024302.
(70) Korotaev, P.; Belov, M.; Yanilkin, A. Reproducibility of vibrational free energy by different methods. *Comput. Mater. Sci.* **2018**, *150*, 47−53.
(71) Ladygin, V.; Korotaev, P.; Yanilkin, A.; Shapeev, A. Lattice dynamics simulation using machine learning interatomic potentials. *Comput. Mater. Sci.* **2020**, *172*, 109333.
(72) Galimberti, D. R.; Sauer, J. Chemically Accurate Vibrational Free Energies of Adsorption from Density Functional Theory Molecular Dynamics: Alkanes in Zeolites. *J. Chem. Theory Comput.* **2021**, *17*, 5849−5862.
(73) Wentzcovitch, R. M.; Yu, Y. G.; Wu, Z. Thermodynamic Properties and Phase Relations in Mantle Minerals Investigated by First Principles Quasiharmonic Theory. *Rev. Mineral. Geochem.* **2010**, *71*, 59−98.
(74) Schütt, K. T.; Kessel, P.; Gastegger, M.; Nicoli, K. A.; Tkatchenko, A.; Müller, K.-R. SchNetPack: A Deep Learning Toolbox For Atomistic Systems. *J. Chem. Theory Comput.* **2019**, *15*, 448−455.
(75) Filip, M. R.; Eperon, G. E.; Snaith, H. J.; Giustino, F. Steric engineering of metal-halide perovskites with tunable optical band gaps. *Nat. Commun.* **2014**, *5*, 5757.
(76) Lin, S.-T.; Blanco, M.; Goddard, W. A. The two-phase model for calculating thermodynamic properties of liquids from molecular dynamics: Validation for the phase diagram of Lennard-Jones fluids. *J. Chem. Phys.* **2003**, *119*, 11792−11805.
(77) Chen, G. P.; Voora, V. K.; Agee, M. M.; Balasubramani, S. G.; Furche, F. Random-Phase Approximation Methods. *Annu. Rev. Phys. Chem.* **2017**, *68*, 421−445.
(78) Harl, J.; Kresse, G. Accurate Bulk Properties from Approximate Many-Body Techniques. *Phys. Rev. Lett.* **2009**, *103*, 056401.
(79) Ren, X.; Rinke, P.; Joas, C.; Scheffler, M. Random-phase approximation and its applications in computational chemistry and materials science. *J. Mater. Sci.* **2012**, *47*, 7447−7471.
(80) Marini, A.; Garcìa-Gonzàlez, P.; Rubio, A. First-Principles Description of Correlation Effects in Layered Materials. *Phys. Rev. Lett.* **2006**, *96*, 136404.
(81) Lebègue, S.; Harl, J.; Gould, T.; Àngyàn, J. G.; Kresse, G.; Dobson, J. F. Cohesive Properties and Asymptotics of the Dispersion Interaction in Graphite by the Random Phase Approximation. *Phys. Rev. Lett.* **2010**, *105*, 196401.
(82) Schimka, L.; Harl, J.; Stroppa, A.; Grüneis, A.; Marsman, M.; Mittendorfer, F.; Kresse, G. Accurate surface and adsorption energies from many-body perturbation theory. *Nat. Mater.* **2010**, *9*, 741−744.
(83) Olsen, T.; Yan, J.; Mortensen, J. J.; Thygesen, K. S. Dispersive and Covalent Interactions between Graphene and Metal Surfaces from the Random Phase Approximation. *Phys. Rev. Lett.* **2011**, *107*, 156401.
(84) Björkman, T.; Gulans, A.; Krasheninnikov, A. V.; Nieminen, R. M. van der Waals Bonding in Layered Compounds from Advanced Density-Functional First-Principles Calculations. *Phys. Rev. Lett.* **2012**, *108*, 235502.
(85) Schimka, L.; Gaudoin, R.; Klimeš, J.; Marsman, M.; Kresse, G. Lattice constants and cohesive energies of alkali, alkaline-earth, and transition metals: Random phase approximation and density functional theory results. *Phys. Rev. B* **2013**, *87*, 214102.
(86) Macher, M.; Klimeš, J.; Franchini, C.; Kresse, G. The random phase approximation applied to ice. *J. Chem. Phys.* **2014**, *140*, 084502.
(87) Kaltak, M.; Klimeš, J.; Kresse, G. Cubic scaling algorithm for the random phase approximation: Self-interstitials and vacancies in Si. *Phys. Rev. B* **2014**, *90*, 054115.
(88) Cui, Z.-H.; Wu, F.; Jiang, H. First-principles study of relative stability of rutile and anatase TiO_2 using the random phase approximation. *Phys. Chem. Chem. Phys.* **2016**, *18*, 29914−29922.
(89) Zhang, M.-Y.; Cui, Z.-H.; Jiang, H. Relative stability of FeS_2 polymorphs with the random phase approximation approach. *J. Mater. Chem. A* **2018**, *6*, 6606−6616.
(90) Klimeš, J.; Kaltak, M.; Maggio, E.; Kresse, G. Singles correlation energy contributions in solids. *J. Chem. Phys.* **2015**, *143*, 102816.
(91) Mattoni, A.; Filippetti, A.; Saba, M. I.; Delugas, P. Methylammonium Rotational Dynamics in Lead Halide Perovskite by Classical Molecular Dynamics: The Role of Temperature. *J. Phys. Chem. C* **2015**, *119*, 17421−17428.
(92) Handley, C. M.; Freeman, C. L. A new potential for methylammonium lead iodide. *Phys. Chem. Chem. Phys.* **2017**, *19*, 2313−2321.
(93) Balestra, S. R. G.; Vicent-Luna, J. M.; Calero, S.; Tao, S.; Anta, J. A. Efficient modelling of ion structure and dynamics in inorganic metal halide perovskites. *J. Mater. Chem. A* **2020**, *8*, 11824−11836.
(94) Chmiela, S.; Sauceda, H. E.; Müller, K.-R.; Tkatchenko, A. Towards exact molecular dynamics simulations with machine-learned force fields. *Nat. Commun.* **2018**, *9*, 3887.
(95) Botu, V.; Batra, R.; Chapman, J.; Ramprasad, R. Machine Learning Force Fields: Construction, Validation, and Outlook. *J. Phys. Chem. C* **2017**, *121*, 511−522.
(96) Jinnouchi, R.; Lahnsteiner, J.; Karsai, F.; Kresse, G.; Bokdam, M. Phase Transitions of Hybrid Perovskites Simulated by Machine-Learning Force Fields Trained on the Fly with Bayesian Inference. *Phys. Rev. Lett.* **2019**, *122*, 225701.
(97) Thomas, J. C.; Bechtel, J. S.; Natarajan, A. R.; Van der Ven, A. Machine learning the density functional theory potential energy surface for the inorganic halide perovskite $CsPbBr_3$. *Phys. Rev. B* **2019**, *100*, 134101.
(98) Chen, H.-A.; Pao, C.-W. Fast and Accurate Artificial Neural Network Potential Model for $MAPbI_3$ Perovskite Materials. *ACS Omega* **2019**, *4*, 10950−10959.
(99) Yang, W.; Li, J.; Chen, X.; Feng, Y.; Wu, C.; Gates, I. D.; Gao, Z.; Ding, X.; Yao, J.; Li, H. Exploring the Effects of Ionic Defects on the Stability of $CsPbI_3$ with a Deep Learning Potential. *ChemPhysChem* **2022**, *23*, No. e202100841.
(100) Friederich, P.; Häse, F.; Proppe, J.; Aspuru-Guzik, A. Machine-learned potentials for next-generation matter simulations. *Nat. Mater.* **2021**, *20*, 750−761.
(101) Kresse, G.; Furthmüller, J. Efficiency of ab-initio total energy calculations for metals and semiconductors using a plane-wave basis set. *Comput. Mater. Sci.* **1996**, *6*, 15−50.
(102) Kresse, G.; Furthmüller, J. Efficient iterative schemes for ab initio total-energy calculations using a plane-wave basis set. *Phys. Rev. B* **1996**, *54*, 11169−11186.
(103) Kresse, G.; Joubert, D. From ultrasoft pseudopotentials to the projector augmented-wave method. *Phys. Rev. B* **1999**, *59*, 1758−1775.
(104) Perdew, J. P.; Burke, K.; Ernzerhof, M. Generalized Gradient Approximation Made Simple. *Phys. Rev. Lett.* **1996**, *77*, 3865−3868.
(105) Grimme, S. Semiempirical GGA-type density functional constructed with a long-range dispersion correction. *J. Comput. Chem.* **2006**, *27*, 1787−1799.
(106) Grimme, S.; Antony, J.; Ehrlich, S.; Krieg, H. A consistent and accurate ab initio parametrization of density functional dispersion correction (DFT-D) for the 94 elements H-Pu. *J. Chem. Phys.* **2010**, *132*, 154104.

https://doi.org/10.1021/acs.chemmater.2c01508
Chem. Mater. 2022, 34, 8561−8576

(107) Grimme, S.; Ehrlich, S.; Goerigk, L. Effect of the damping function in dispersion corrected density functional theory. *J. Comput. Chem.* **2011**, *32*, 1456−1465.
(108) Axilrod, B. M.; Teller, E. Interaction of the van der Waals Type Between Three Atoms. *J. Chem. Phys.* **1943**, *11*, 299−300.
(109) Muto, Y. Force between nonpolar molecules. *Proc. Phys. Math. Soc. Jpn.* **1943**, *17*, 629−631.
(110) Tkatchenko, A.; Scheffler, M. Accurate Molecular Van Der Waals Interactions from Ground-State Electron Density and Free-Atom Reference Data. *Phys. Rev. Lett.* **2009**, *102*, 073005.
(111) Tkatchenko, A.; DiStasio, R. A.; Car, R.; Scheffler, M. Accurate and Efficient Method for Many-Body van der Waals Interactions. *Phys. Rev. Lett.* **2012**, *108*, 236402.
(112) Ambrosetti, A.; Reilly, A. M.; DiStasio, R. A.; Tkatchenko, A. Long-range correlation energy calculated from coupled atomic response functions. *J. Chem. Phys.* **2014**, *140*, 18A508.
(113) Bučko, T.; Lebègue, S.; Gould, T.; Ángyán, J. G. Many-body dispersion corrections for periodic systems: an efficient reciprocal space implementation. *J. Phys.: Condens. Matter* **2016**, *28*, 045201.
(114) Gould, T.; Lebègue, S.; Ángyán, J. G.; Bučko, T. A Fractionally Ionic Approach to Polarizability and van der Waals Many-Body Dispersion Calculations. *J. Chem. Theory Comput.* **2016**, *12*, 5920−5930.
(115) Csonka, G. I.; Perdew, J. P.; Ruzsinszky, A.; Philipsen, P. H. T.; Lebègue, S.; Paier, J.; Vydrov, O. A.; Ángyán, J. G. Assessing the performance of recent density functionals for bulk solids. *Phys. Rev. B* **2009**, *79*, 155107.
(116) Dion, M.; Rydberg, H.; Schröder, E.; Langreth, D. C.; Lundqvist, B. I. Van der Waals Density Functional for General Geometries. *Phys. Rev. Lett.* **2004**, *92*, 246401.
(117) Lee, K.; Murray, E. D.; Kong, L.; Lundqvist, B. I.; Langreth, D. C. Higher-accuracy van der Waals density functional. *Phys. Rev. B* **2010**, *82*, 081101.
(118) Klimeš, J.; Bowler, D. R.; Michaelides, A. Van der Waals density functionals applied to solids. *Phys. Rev. B* **2011**, *83*, 195131.
(119) Klimeš, J.; Bowler, D. R.; Michaelides, A. Chemical accuracy for the van der Waals density functional. *J. Phys.: Condens. Matter* **2010**, *22*, 022201.
(120) Sun, J.; Ruzsinszky, A.; Perdew, J. P. Strongly Constrained and Appropriately Normed Semilocal Density Functional. *Phys. Rev. Lett.* **2015**, *115*, 036402.
(121) Peng, H.; Yang, Z.-H.; Perdew, J. P.; Sun, J. Versatile van der Waals Density Functional Based on a Meta-Generalized Gradient Approximation. *Phys. Rev. X* **2016**, *6*, 041005.
(122) Zhao, Y.; Truhlar, D. G. A new local density functional for main-group thermochemistry, transition metal bonding, thermochemical kinetics, and noncovalent interactions. *J. Chem. Phys.* **2006**, *125*, 194101.
(123) Heyd, J.; Scuseria, G. E.; Ernzerhof, M. Hybrid functionals based on a screened Coulomb potential. *J. Chem. Phys.* **2003**, *118*, 8207−8215.
(124) Krukau, A. V.; Vydrov, O. A.; Izmaylov, A. F.; Scuseria, G. E. Influence of the exchange screening parameter on the performance of screened hybrid functionals. *J. Chem. Phys.* **2006**, *125*, 224106.
(125) Steiner, S.; Khmelevskyi, S.; Marsmann, M.; Kresse, G. Calculation of the magnetic anisotropy with projected-augmented-wave methodology and the case study of disordered $Fe_{1-x}Co_x$ alloys. *Phys. Rev. B* **2016**, *93*, 224425.
(126) Janssen, J.; Surendralal, S.; Lysogorskiy, Y.; Todorova, M.; Hickel, T.; Drautz, R.; Neugebauer, J. pyiron: An integrated development environment for computational materials science. *Comput. Mater. Sci.* **2019**, *163*, 24−36.
(127) Hoover, W. G.; Ladd, A. J. C.; Moran, B. High-Strain-Rate Plastic Flow Studied via Nonequilibrium Molecular Dynamics. *Phys. Rev. Lett.* **1982**, *48*, 1818−1820.
(128) Evans, D. J. Computer "experiment" for nonlinear thermodynamics of Couette flow. *J. Chem. Phys.* **1983**, *78*, 3297−3302.
(129) Kaltak, M.; Klimeš, J.; Kresse, G. Cubic scaling algorithm for the random phase approximation: Self-interstitials and vacancies in Si. *Phys. Rev. B* **2014**, *90*, 054115.
(130) Kaltak, M.; Klimeš, J.; Kresse, G. Low Scaling Algorithms for the Random Phase Approximation: Imaginary Time and Laplace Transformations. *J. Chem. Theory Comput.* **2014**, *10*, 2498−2507.
(131) Harl, J.; Schimka, L.; Kresse, G. Assessing the quality of the random phase approximation for lattice constants and atomization energies of solids. *Phys. Rev. B* **2010**, *81*, 115126.
(132) Hutter, J.; Iannuzzi, M.; Schiffmann, F.; VandeVondele, J. CP2K: atomistic simulations of condensed matter systems. *Wiley Interdiscip. Rev. Comput. Mol. Sci.* **2014**, *4*, 15−25.
(133) VandeVondele, J.; Krack, M.; Mohamed, F.; Parrinello, M.; Chassaing, T.; Hutter, J. Quickstep: Fast and accurate density functional calculations using a mixed Gaussian and plane waves approach. *Comput. Phys. Commun.* **2005**, *167*, 103−128.
(134) Lippert, B. G.; Hutter, J.; Parrinello, M. A hybrid Gaussian and plane wave density functional scheme. *Mol. Phys.* **1997**, *92*, 477−488.
(135) Goedecker, S.; Teter, M.; Hutter, J. Separable dual-space Gaussian pseudopotentials. *Phys. Rev. B* **1996**, *54*, 1703−1710.
(136) VandeVondele, J.; Hutter, J. Gaussian basis sets for accurate calculations on molecular systems in gas and condensed phases. *J. Chem. Phys.* **2007**, *127*, 114105.
(137) Nosé, S. A unified formulation of the constant temperature molecular dynamics methods. *J. Chem. Phys.* **1984**, *81*, 511−519.
(138) Nosé, S. A molecular dynamics method for simulations in the canonical ensemble. *Mol. Phys.* **1984**, *52*, 255−268.
(139) Hoover, W. G. Canonical dynamics: Equilibrium phase-space distributions. *Phys. Rev. A* **1985**, *31*, 1695−1697.
(140) Martyna, G. J.; Tobias, D. J.; Klein, M. L. Constant pressure molecular dynamics algorithms. *J. Chem. Phys.* **1994**, *101*, 4177−4189.
(141) Kingma, D. P.; Ba, J.Adam: A Method for Stochastic Optimization. *arXiv*, 2017-1-30; https://arxiv.org/abs/1412.6980.
(142) Schütt, K. T.; Sauceda, H. E.; Kindermans, P.-J.; Tkatchenko, A.; Müller, K.-R. SchNet − A deep learning architecture for molecules and materials. *J. Chem. Phys.* **2018**, *148*, 241722.

https://doi.org/10.1021/acs.chemmater.2c01508
Chem. Mater. 2022, 34, 8561−8576